Unusual plasma and particle signatures at Mars and STEREO-A related to CME-CME interaction

Mateja Dumbović,[1] Jingnan Guo,[2,3] Manuela Temmer,[1] M. Leila Mays,[4] Astrid Veronig,[1,5]
Stephan Heinemann,[1] Karin Dissauer,[1] Stefan Hofmeister,[1] Jasper Halekas,[6] Christian Möstl,[7]
Tanja Amerstorfer,[7] Jürgen Hinterreiter,[7,1] Saša Banjac,[3] Konstantin Herbst,[3] Yuming Wang,[2]
Lukas Holzknecht,[1] Martin Leitner,[1] and Robert F. Wimmer–Schweingruber[3]

[1]*Institute of Physics, University of Graz, Universitätsplatz 5, A-8010 Graz, Austria*
[2]*CAS Key Laboratory of Geospace Environment, School of Earth and Space Sciences, University of Science and Technology of China,
Hefei, China*
[3]*Department of Extraterrestrial Physics, Christian-Albrechts University in Kiel, Leibnitzstrasse 11, 24098, Kiel, Germany*
[4]*NASA Goddard Space Flight Center, Greenbelt, MD 20771, USA*
[5]*Kanzelhöhe Observatory for Solar and Environmental Research, University of Graz, Kanzelhöhe 19, 9521 Treffen, Austria*
[6]*Department of Physics and Astronomy, University of Iowa, Iowa City, IA 52242, USA*
[7]*Space Research Institute, Austrian Academy of Sciences, Schmiedlstrae 6, 8042 Graz, Austria*

ABSTRACT

On July 25 2017 a multi-step Forbush decrease (FD) with the remarkable total amplitude of more than 15% was observed by MSL/RAD at Mars. We find that these particle signatures are related to very pronounced plasma and magnetic field signatures detected in situ by STEREO-A on July 24 2017, with a higher than average total magnetic field strength reaching more than 60 nT. In the observed time period STEREO-A was at a relatively small longitudinal separation (46 degrees) to Mars and both were located at the back side of the Sun as viewed from Earth. We analyse a number of multi-spacecraft and multi-instrument (both in situ and remote-sensing) observations, and employ modelling to understand these signatures. We find that the solar sources are two CMEs which erupted on July 23 2017 from the same source region on the back side of the Sun as viewed from Earth. Moreover, we find that the two CMEs interact non-uniformly, inhibiting the expansion of one of the CMEs in STEREO-A direction, whereas allowing it to expand more freely in the Mars direction. The interaction of the two CMEs with the ambient solar wind adds up to the complexity of the event, resulting in a long, sub-structured interplanetary disturbance at Mars, where different sub-structures correspond to different steps of the FD, adding-up to a globally large-amplitude FD.

Keywords: solar-terrestrial relations — Sun: coronal mass ejections (CMEs)

1. INTRODUCTION

Interplanetary counterparts of coronal mass ejections (ICMEs) are the most prominent short-term transient phenomena in the heliosphere which significantly influence the interplanetary space and can have major impact on Earth and other planets (see an overview by Kilpua et al. 2017, and references therein). The Heliophysics System Observatory[1] enables us to observe ICME-related signatures at different heliospheric positions and, combined with remote observations as well as modelling efforts, to better understand the propagation and evolution of ICMEs. Recently, an ICME (*i.e.* its shock signatures) was tracked and modelled all the way from the Sun to the outer heliosphere (Witasse et al. 2017), using, among other things, Forbush decreases (FDs) as ICME signatures.

Corresponding author: Mateja Dumbović
mateja.dumbovic@uni-graz.at

Corresponding author: Jingnan Guo
jnguo@ustc.edu.cn

[1] https://www.nasa.gov/content/goddard/heliophysics-system-observatory-hso

FDs are observed as short-term depressions in the galactic cosmic ray flux (Forbush 1937; Hess and Demmelmair 1937), with onset corresponding to the ICME arrival (Cane et al. 1996; Dumbović et al. 2011). The magnitude, shape, duration as well as the sub-structuring of the FD depend on the physical properties of the corresponding interplanetary transient (for overview see *e.g.* Richardson 2004; Cane 2000; Belov 2009, and references therein) and more specifically, ICME-related FDs are expected to reflect the evolutionary properties of ICMEs, such as expansion (Dumbović et al. 2018a). Therefore, they are highly suitable as ICME signatures and are used to indicate ICME arrival *when* and *where* other *in situ* measurements are unavailable (*e.g.* in pre-satellite era or at Mars, see Möstl et al. 2015; Lefèvre et al. 2016; Vennerstrom et al. 2016; Freiherr von Forstner et al. 2018; Winslow et al. 2018). From that perspective, the Radiation Assessment Detector (RAD, Hassler et al. 2012), on board Mars Science Laboratory's (MSL) rover Curiosity (Grotzinger et al. 2012) was shown to be highly suitable for identifying ICMEs' arrival at Mars with detected FDs (Guo et al. 2018b).

While trying to understand the basic physics, often single and simple, text–book example ICMEs are analysed, but it is important to note that the frequency of such events can be relatively low. Many *in situ* detected ICMEs do not show typical magnetic cloud properties (*i.e.* magnetic field rotation, low plasma beta, low density and temperature, expanding speed profile, see *e.g.* Burlaga et al. 1981; Zurbuchen and Richardson 2006; Kilpua et al. 2017, and references therein), quite likely because of, among other things, CME-CME interactions. CME-CME interactions are expected to be quite common considering the CME occurrence frequency and their typical propagation time (Lugaz et al. 2017) and can lead to more intense geomagnetic storms (Wang et al. 2003b,a; Farrugia et al. 2006a,b; Xie et al. 2006; Lugaz and Farrugia 2014; Shen et al. 2017) as well as larger-amplitude FDs (Papaioannou et al. 2010; Dumbović et al. 2016). Therefore, from the space weather point of view these complex events are especially challenging and interesting to study (see also *e.g.* Webb and Nitta 2017). Moreover, understanding the underlying physics in such events offers an opportunity to improve future modelling efforts and predictions of such strong space weather events.

2. DATA AND METHOD

On July 25 2017 MSL/RAD observed a Forbush decrease (FD) with one of the biggest relative amplitudes detected by this instrument since its launch (Guo et al. 2018b). The FD does not only have an unusually large amplitude, but in addition shows a quite complex time profile, possibly indicating interactions of two or even several interplanetary transients. In order to understand this event and the conditions which lead to these specific signatures we search for possible solar sources, assuming that (1) a very impulsive CME is most likely involved, and (2) CME-CME interaction is very likely.

In a time period 6 days prior to the FD observed at Mars, we search for possible CME candidates. For this we use SOHO/LASCO (Brueckner et al. 1995) coronagraphs C2 and C3, with field-of-view reaching 6 $R_\odot$ and 32 $R_\odot$, respectively, and STEREO-A(ST-A)/SECCHI (Howard et al. 2008) EUVI/COR1/COR2 image data with field-of-view reaching 1.7 $R_\odot$, 2.5 $R_\odot$ and 15 $R_\odot$, respectively. We find only 4 CMEs that have a position angle relating to Mars direction, which was almost in the oposition. The first two CMEs launched on July 20, and the other two launched about two days later, around the beginning of July 23 and were much stronger and faster. The last of these 4 CMEs is extremely fast and wide and is very likely interacting with a preceding CME launched shortly before. As the separation angle between ST-A and Mars is not large (46°), we check possible ICME signatures measured at ST-A for more insight on these ICME characteristics. For this we use the PLASTIC (Galvin et al. 2008) and IMPACT (Acuña et al. 2008) *in situ* plasma and magnetic field instruments. Indeed, we find a very pronounced *in situ* magnetic cloud signature on July 24 2017 with a magnetic field strength reaching more than 60 nT.

The two CMEs that erupted on July 23 are the most likely candidates of the signatures observed both in MSL/RAD and ST-A/PLASTIC+IMPACT as they best match the timing and direction for causing the observed FD at Mars. Therefore, in the following we focus on these two CMEs, here forth denoted as CME1 and CME2. The other two CMEs, launched on July 20, are discussed later in the frame of background solar wind effects and are denoted as CMEs 0.1 and 0.2. We hypothesise that the unusual observational signatures are due to the interaction of CMEs 1 and 2. To test this hypothesis we employ a number of multi-spacecraft and multi-instrument observations, as well as modelling. We note that the observational methods and models we use to test the hypothesis suffer from a number of uncertainties, therefore, constructing a plausible explanation of this complex event is challenging. Nevertheless, we argue that the combined synergetic view of the results and interpretations obtained from different models and observations indicates the most likely explanation.
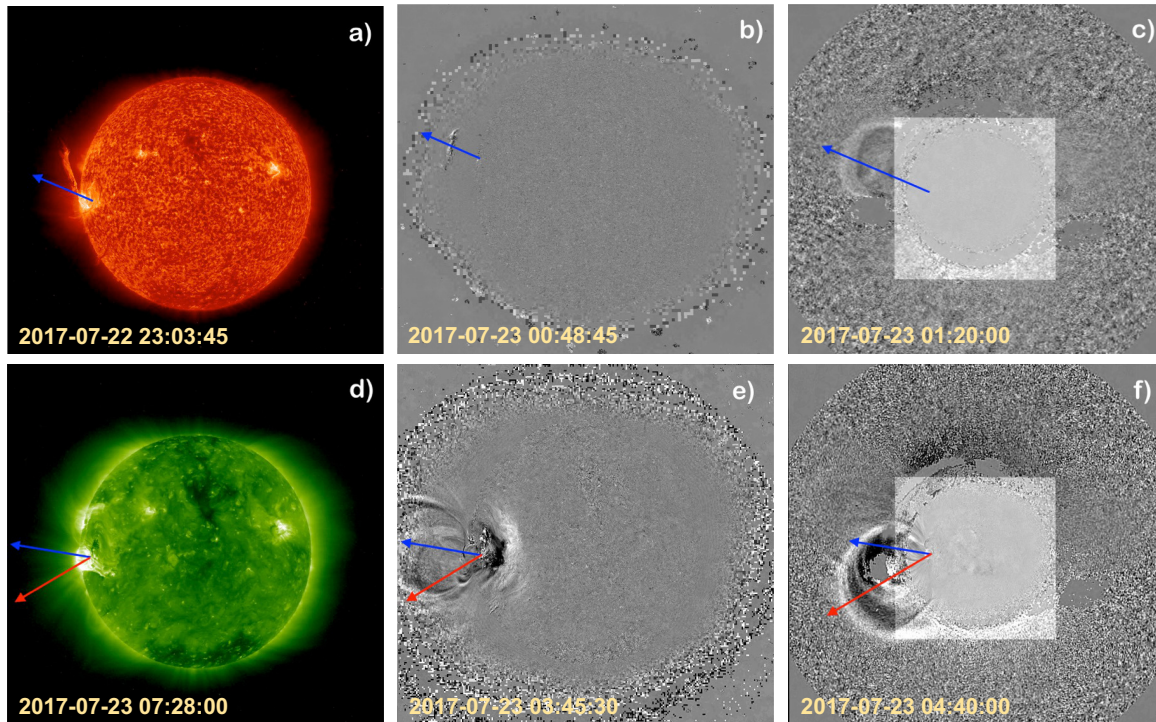
2.1. *CME observations*

Figure 1. Low coronal eruption signatures associated with CMEs 1 and 2: a) a prominence eruption associated with CME1 observed by ST-A/EUVI 304 Å; b) running difference image of ST-A/EUVI 304 Å showing prominence moving radially outward; c) running difference images of ST-A/EUVI 304 Å and ST-A/COR1 showing CME1; d) post-flare loops associated with CME2 observed by ST-A/EUVI 195 Å; e) running difference image of ST-A/EUVI 195 Å with erupting loops associated to CME2; f) running difference images of ST-A/EUVI 195 Å and ST-A/COR1 showing the "main" part of CME2. Blue arrow in a-c marks the direction of the CME1 eruption. Red and blue arrows in d-f mark the directions of multi–step eruptions observed in ST-A/EUVI (For detailed explanation see main text. *Credit: JHelioviewer*).

A filament/prominence eruption starts around 22:30 UT on July 22 2017 observed by ST-A/EUVI 304 Å (Figure 1a), where one part of the filament continues to move radially outward (Figure 1b) and can be observed as CME in COR1 at around 01:05 UT on July 23 2017 with the same (northward) direction of motion (Figure 1c). The source region appears to be AR 12665 at the east limb of ST-A's field of view with approximate Stonyhurst coordinates [0,155]. The CME (henceforth CME1) is observed in COR2 at 01:55 UT, and appears in LASCO/C2 field of view at 01:36 UT.

In order to more reliably derive the direction and geometry of the CME, we use coronagraphic images from different vantage points, ST-A and LASCO, to perform a 3D CME reconstruction using the Graduated cylindrical shell model (GCS, Thernisien et al. 2006, 2009; Thernisien 2011). GCS assumes that geometrically a CME can be represented as a hollow croissant with origin in the center of the Sun, *i.e.* with conical legs, circular cross section and pseudo-circular front. A projection of the croissant (green mesh in Figure 2) at a given time is fitted to coronagraphic images, where two different vantage points are needed to better constrain the fit. We manually fit the GCS model to the CME observations using ST-A/COR2 and LASCO/C3 images from 03:06 and 03:08 UT respectively (see Figure 2a). Assuming radial propagation direction, we use as starting position the CME source region, *i.e.* the AR location. The best fit is derived for a direction slightly different from the AR location (Stonyhurst coordinates [10,170]) indicating a deflection towards Mars and ST-A. For obtaining a kinematic profile, we assume self–similar expansion, keep all GCS parameters, except for height, constant and fit stereoscopic images for several time steps. We note that for later time steps we cannot find a good match anymore for the CME front as it deforms most probably due to a helmet streamer (see Figure 2b).

As CME1 exits ST-A/COR2 field of view around 03:20 UT, an eruption is observed in the same AR 12665 at the east limb in ST-A/EUVI 195 Å, followed by a dimming, an EUV wave and post-flare loops (fig 1d). A more detailed analysis of the EUVI observations reveals a multi–step eruption, where several eruptions are observed very closely in time in the same AR. We first observe erupting loops in EUVI, appearing also in COR1 but as very faint structures
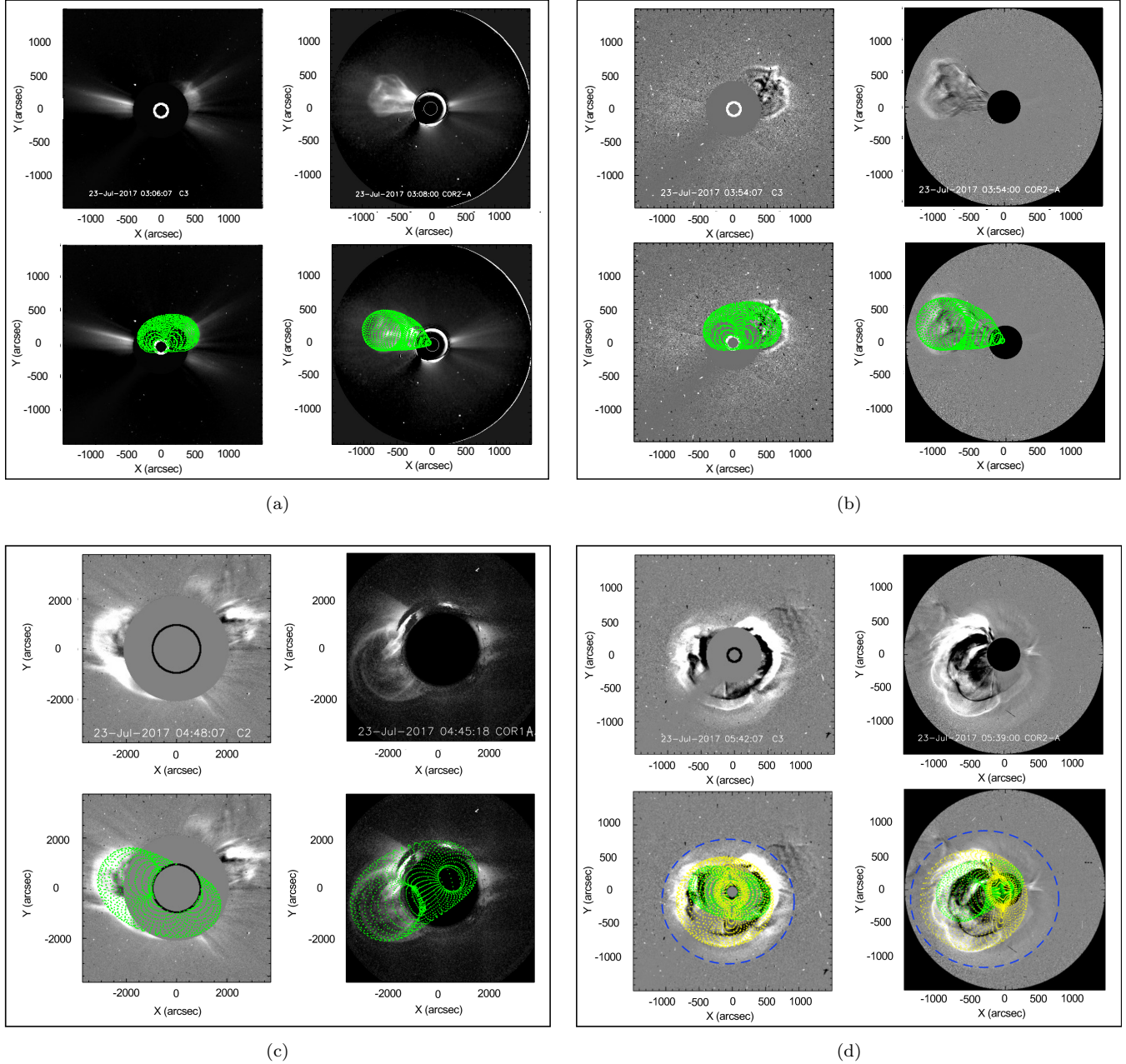
Figure 2. GCS reconstructions of CMEs 1 and 2 at different times: a) when the CME1 leading edge can be fitted with a croissant ($R = 11.6$ R$_\odot$); b) when the leading edge of CME1 cannot be perfectly fitted anymore($R = 14.9$ R$_\odot$); c) the "main" part of CME2 fitted with a croissant model (in C2 and COR1, $R = 4.25$ R$_\odot$); d) a multi–step complex CME2 fitted with a quasi-sphere (in C3 and COR2, $R = 19.2$ R$_\odot$). The green mesh outlines the fitted croissant both for CME 1 and 2, the yellow wire outlines a fitted quasi-sphere for CME2 and the blue dashed circle outlines the shock front. Reconstruction parameters for both CMEs are given in Table 2.

and are oriented northward (blue arrow in Figure 1d-e). The second eruption observed in EUVI is associated with a strong EUV wave and is seen as a very prominent structure in COR1 moving more southward (red arrow in Figure 1d-e). The third eruption is associated with a strong flare, is narrow, and the most impulsive. In COR1 it is not easily distinguishable from the second eruption, however, it can be seen as a localised emission enhancement, where its outer structure overlap with the Northern loops segment of the previous eruption. For a more detailed analysis of the early multi–eruption signatures we refer the reader to a study by Liu et al. (2019). The single eruptions cannot

be individually tracked and appear to move as one entity already in COR1 field-of-view. In COR2 field-of-view the structures appear as a single CME. Therefore, in the further analysis we treat this as a multi–step eruption resulting in a single CME. The CME (henceforth CME2) is detected by COR2 at 04:54 UT, and appears in the LASCO/C2 field of view at 04:45 UT.

We perform a GCS reconstruction of the CME main part in ST-A/COR1 and LASCO/C2 images at 04:45 and 04:48, respectively, where the CME can be reasonably fitted by a croissant model (green mesh in Figure 2c). However, in the field of view of COR2 and C3 the simple croissant geometry does not match anymore with the observed CME structure, and a best fit would be obtained for a quasi–spherical geometry (yellow mesh in Figure 2d)[2]. Even by introducing deflection, rotation and non–self–similar expansion it is impossible to obtain a reasonable transition from the croissant fitted in COR1 to the quasi–sphere fitted in COR2. This reflects the interaction of these multiple eruptions very early in their evolution. We therefore abandon the "main" eruption part fitted in COR1/C2 and for obtaining the kinematics of CME2 track the quasi–spherical bright structure, which we extrapolate back and forward in time assuming self-similar expansion and radial propagation.

2.2. In situ observations at STEREO-A

In Figure 3 ST-A/IMPACT and PLASTIC *in situ* magnetic field and plasma data are shown in a time period 24–28 July 2017. The *in situ* event shows quite complex signatures, where several different regions can be identified using standard observational criteria described by *e.g.* Zurbuchen and Richardson (2006); Richardson and Cane (2010); Kilpua et al. (2017); Richardson (2018). The start of the event can be identified on July 24 (DOY 205) around 13:15 UT with a simultaneous jump in magnetic field, temperature, density and speed followed by the typical sheath characteristics - elevated temperature, density, speed and plasma beta and fluctuating magnetic field (region 1 in Figure 3). Although the elevated values do not seem prominent compared to the rest of the interval (extreme parameter values in regions 3 and 4) we note that the magnetic field increases from around 3 nT to around 11 nT, a jump comparable to typical events. Therefore, we identify this region as the shock/sheath region.

In region 2 we also observe typical sheath characteristics, however they are much stronger than in region 1: the magnetic field strength is on average 4–5 times stronger, density is about 6 times higher, temperature 2–3 times higher and there is an increase of flow speed throughout the region from about 550 km s^{-1} to 660 km s^{-1}. This might indicate a second shock/sheath region or a continuation of one common sheath where the plasma and magnetic field are strongly piled up against the strong magnetic field of the magnetic structure in the region that follows (region 3). However, due to the data gap between region 1 and 2, this can not be fully resolved.

In region 3 qualitatively typical magnetic cloud (MC) signatures are observed – strong and smoothly rotating magnetic field, low density, temperature and plasma beta, however quantitatively this MC is quite unusual. The magnetic field strength is extremely high, at its peak (~ 65 nT) it is 6 times higher than MC values typically observed at 1 AU (10 nT at Earth, see Richardson and Cane 2010), the MC duration (~ 7 hours) is on the other hand extremely short, around 4 times shorter than MC durations typically observed at 1 AU (around 30 hours, see Richardson and Cane 2010), and finally, the flow speed does not show a typical linearly decreasing (expansion) profile. These are strong indications that the expansion of this CME was inhibited. We perform the Lundquist fitting to the magnetic field data (Leitner et al. 2007) and find a reasonable fit (green curves in Figure 3b) with orientation showing a $-13°$ axis tilt to ecliptic, central magnetic field of 40 nT and an estimated diameter of 0.12 AU, *i.e.* 26 R$_\odot$. There is a quite large discrepancy of the fit and data at the beginning of the MC, as the magnetic field shows a quite asymmetric profile, not unusual for the fast CMEs (Masías-Meza et al. 2016), which might be due to a plasma/magnetic field line pile–up within the MC near the leading edge.

In region 4 we observe a typical stream interface signature – drop of density followed by the increase in temperature and speed, the fluctuating and elevated magnetic field and small spike in the plasma beta, a common feature of stream interaction regions (SIRs). This is however not followed by the typical high speed stream (HSS) signatures in region 5, where high flow speed is accompanied with a relatively low temperature, plasma beta and density. The speed which peaks on the front with about 800 km s^{-1} shows a highly expanding profile with speed at the trailing edge reaching 400 km s^{-1}, and the duration of the region is about 50h, which is quite long compared to typical ICME duration at 1 AU (around 30 hours, see Richardson and Cane 2010). The magnetic field is relatively smooth but weak and shows no obvious rotation, although there are indications of sub-structuring. These might be indications of a highly expanded

---

[2] We note that it is unlikely that this bright structure is a shock, as the typical shock signature is a faint front (Vourlidas et al. 2013) which we observe propagating ahead (blue dashed circle in Figure 2d)

CME, a specific trajectory of the spacecraft through the leg of the CME (see *e.g.* Möstl et al. 2010), or of a complex ejecta/compound stream (see e.g. Burlaga et al. 2003; Lugaz et al. 2017).

2.3. *In situ observations at Mars*

In Figure 3 MAVEN (Mars Atmosphere and Volatile EvolutioN, Jakosky et al. 2015) *in situ* magnetic field and plasma data, as well as MSL/RAD relative count rates are shown in a time period 24 July – 7 August 2017. To avoid contamination from measurements taken inside the bow shock we use an algorithm described by Halekas et al. (2017). Similar as at STEREO-A, the *in situ* event at Mars shows quite complex signatures, where several different regions can be identified. We note that the identification here is not so straightforward as with ST-A, due to uneven coverage of the solar wind. We interpolate the measurements to guide the eye, however, we note that one has to be careful not to misinterpret the interpolation for measurements. Nevertheless, using MAVEN in combination with MSL/RAD data, which provides additional information on the associated Forbush decreases, we are able to identify different sub-structures. For that purpose we use sol–filtered MSL/RAD data in which the daily pressure–induced oscillations have been removed (for details on the method see Guo et al. 2018b). As a proxy of the CR count we use relative values of the dose rate normalised to the beginning of the observed period.

Region 1 is characterised by, what appears to be typical stream interface properties with a corresponding decrease in GCRs of about 4% as detected by MSL/RAD which starts July 25 around 00:00 UT. Unfortunately, MAVEN was not measuring the solar wind plasma and magnetic field throughout region 2, however we do discern this as a separate region due to two reasons. Firstly, the plasma speed and the B_y component show distinctively different properties at the start and end of this gap. Secondly, MSL/RAD data show an increase of 5% at the start of this region, followed by a rapid decrease of 5% (measured from the onset point, not the peak point) which are typical shock/sheath-related FD properties (*e.g.* Cane 2000). Therefore, we suggest that this is most likely a shock/sheath region, where the speed increase throughout the region indicates that the shock is still driven.

Region 3 is characterised by a relatively low plasma beta and what appears to be a decreasing speed profile indicating expansion of the magnetic structure. The magnetic field also seems to be somewhat elevated, however, due to the data gap in the first half-period it is not possible to make a reliable estimation about the strength or rotation of the magnetic field. MSL/RAD on the other hand shows a start of another, less rapid decrease at the beginning of this region which might indicate the beginning of the ejecta–related FD. However, the depression does not return to the onset value but is "interrupted" by another decrease at the start of region 4. In region 4 we again identify what appears to be stream interface signatures, however, the reliability is questionable due to the MAVEN data gap and moreover MSL/RAD data show a double–decrease structure which indicates that this region might not be a simple stream interface region.

Region 5 is again characterised by an expanding speed profile, the plasma beta is not low at the very start of the region, but drops later. In the second part where the MAVEN data are more consistent, the magnetic field components show a relatively smooth profile, although the magnetic field strength is not really elevated. These are characteristics similar to CME2 identified in ST-A. Finally, in region 6 we observe elevated temperature and speed, which are the typical HSS signatures.

We note that the whole period encompassing *in situ* regions 1–6 correspond to a single, long–duration multi–step FD, where different regions (*i.e.* substructures) correspond to different steps of the FD. The unusually large FD amplitude might therefore be related to the complexity of the event, where different steps add–up into a single global FD, as suggested by some previous studies (*e.g.* Papaioannou et al. 2010; Dumbović et al. 2016).

3. RESULTS

3.1. *Pre-conditioning of the heliospheric background*

In order to analyse and understand the propagation and interaction of CMEs 1 and 2 it is imperative to analyse and understand the heliospheric background. For that purpose we check the remote ST-A observations prior to CME 1 and 2 eruptions to identify any relevant coronal holes (CHs) and/or CMEs that might act to pre-condition the interplanetary space. As can be seen in Figure 1d there is a CH passing the central meridian as seen from ST-A on the day of the eruptions (CH1, see Figure 4a). Visually, the CH area crossing the central meridian slice does not appear very large and thus we do not expect the corresponding HSS to be very fast (Nolte et al. 1976; Vršnak et al. 2007; Tokumaru et al. 2017; Hofmeister et al. 2018). Therefore, it might be likely that the two CMEs "catch-up" with the SIR corresponding to CH1, which might influence their propagation. We observe another possibly relevant CH which
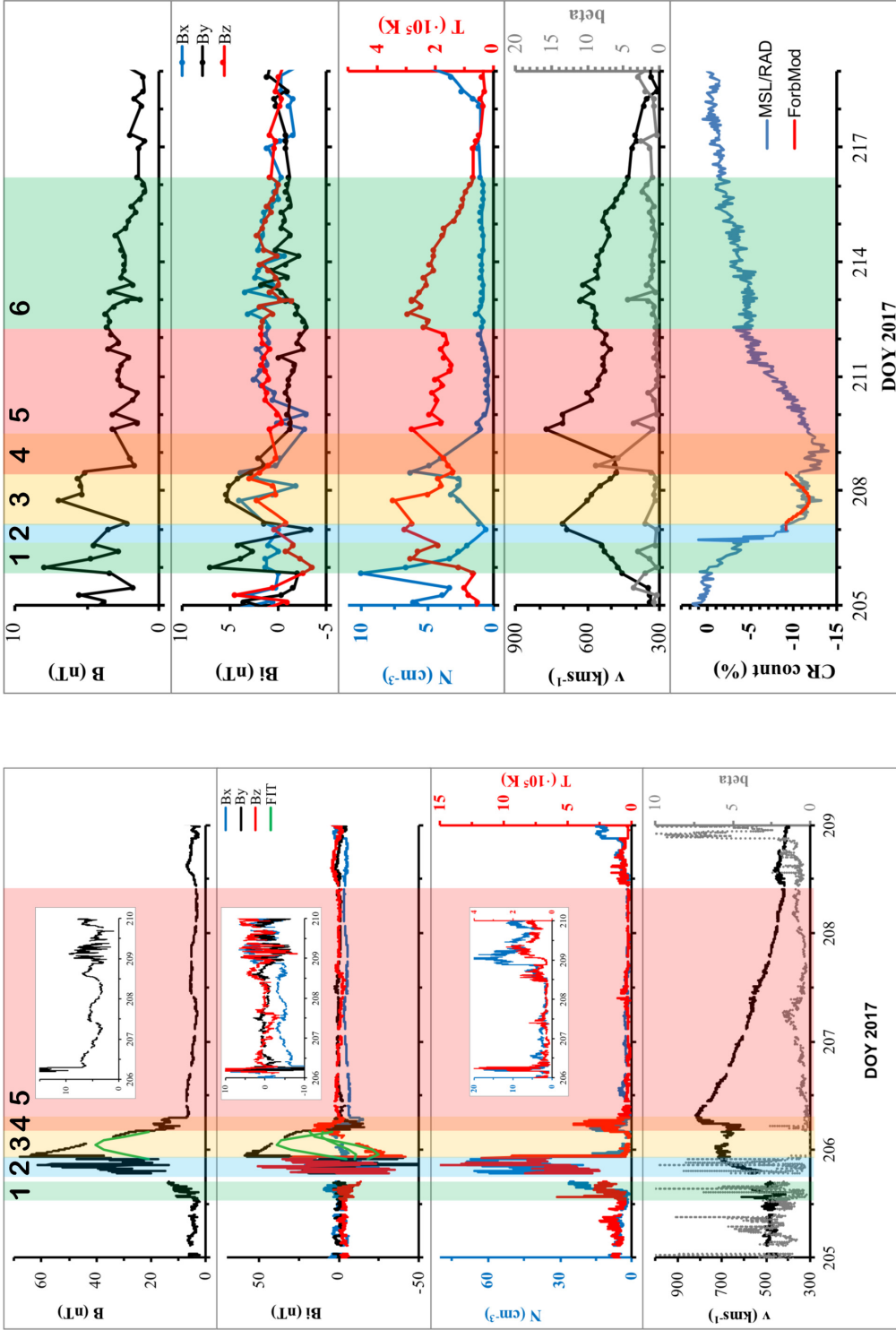
Figure 3. *In situ* measurements at ST-A and Mars:

Left: ST-A/PLASTIC+IMPACT measurements for July 24–28 (DOY 205–209) with top-to-bottom panels showing magnetic field components, B_x, B_y, and B_z, plasma density, N, plasma temperature, T, and plasma beta and speed, v. Differently coloured shading outlines different regions (1–5, for explanation see main text). Small panels embedded in top three larger panels show a zoomed-in region 5 (DOY 206–210). The green curves in top two panels mark the Lundquist fit (hourly values, χ^2-test p-value is 0.011).

Right: MAVEN and MSL/RAD measurements for July 24 – August 7 (DOY 205–219) with top-to-bottom panels showing magnetic field strength, B, three magnetic field components, B_x, B_y, and B_z, plasma density, N and temperature, T, plasma beta and speed, v, and GCR count proxy by MSL/RAD. Differently coloured shading outlines different regions (1–6, for explanation see main text). The red curve in the bottom plot marks the ForbMod fit (Forbush decrease model, for explanation see section 3.3).
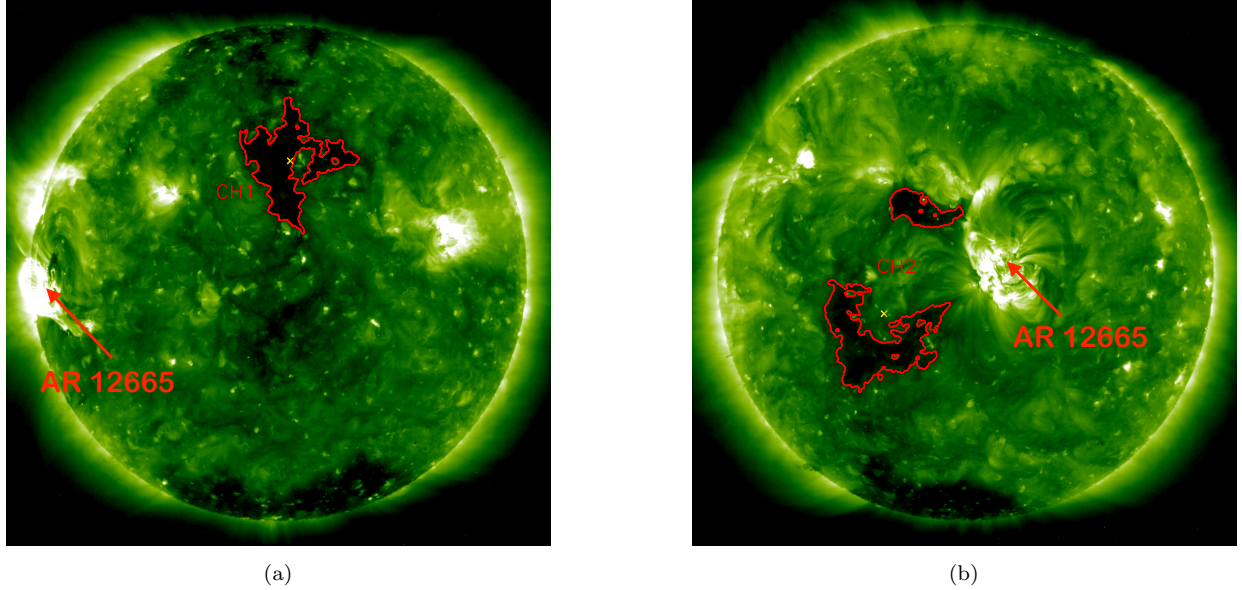
(a)   (b)

Figure 4. CH1 (a) and CH2 (b) in EUVI/ST-A 195 Å crossing the central meridian as observed from ST-A July 23 and July 29, respectively. The red contours mark outline the CHs and the yellow x marks the center of mass of the the CH. The arrow points to AR 12665, which is the source region of CMEs 1 and 2.

Table 1. CH area values and peak speed of the associated solar wind calculated using the CH area – SW speed from different studies.

	CH1	CH2 (top)	CH2 (bottom)	CH2 (full)
$A[10^{10}\mathrm{km}^2]$	4.8 ± 0.3	1.28 ± 0.05	5.3 ± 0.4	6.5 ± 0.5
$v[\mathrm{~km~s}^{-1}]$ (Hofmeister et al. 2018)	552 ± 4	505 ± 1	588 ± 9	630 ± 10
$v[\mathrm{~km~s}^{-1}]$ (Tokumaru et al. 2017)	476^{+5}_{-3}	462 ± 3	477^{+7}_{-3}	483^{+7}_{-3}
$v[\mathrm{~km~s}^{-1}]$ (Nolte et al. 1976)	790^{+60}_{-10}	525^{+15}_{-7}	810^{+80}_{-20}	910^{+90}_{-20}

is at the time of the eruption behind the eastern limb as viewed from ST-A (CH2, see Figure 4b). CH2 is "trailing" the eruption site, however due to its vicinity to the active region might interact with the eruptions through interchange reconnection (*e.g.* Crooker et al. 2002). In Figure 4 CH1 and CH2 are shown at the time crossing the central meridian as observed from ST-A, where their corresponding area is extracted using a thresholding technique based on the study by Heinemann et al. (2018b,a). The CH area values are presented in Table 1 for both CHs. CH2 consists of the top and bottom part, therefore we present three area calculations: for the top part only, for the bottom part only and for both (full). In addition, based on the calculated area we calculate the peak speed of the associated solar wind using the CH area – SW speed relations given by Nolte et al. (1976) and Tokumaru et al. (2017), as well as latitude dependent CH area – SW speed relation by Hofmeister et al. (2018). These are also presented in Table 1. It can be seen that the HSS originating from CH1 is most probably slower than CMEs 1 and 2, hence, a kinematical interaction between them is likely. It can also be seen that CH2 is expected to yield a faster streams than CH1, therefore although the angular separation between the two is roughly 90°, if undisturbed we would expect the time difference between two corresponding SIR to be < 7 days.

In section 2 we noted that in addition to CMEs 1 and 2 we observed two more CMEs that have a position angle relating to Mars direction. These two CMEs (marked as CME0.1 and CME0.2) erupted from the same AR on July 20 2017, and might therefore be important for pre-conditioning of the interplanetary space (Temmer et al. 2017; Temmer and Nitta 2015), especially in the direction of Mars. In Figure 5 we present the GCS reconstruction of these two CMEs. CME0.1 starts with loop motions observed at the east limb in the ST-A EUVI 195 Å, followed by the CME observed in COR1 at 13:25 UT. The CME appears in the ST-A/COR2 and LASCO/C2 field of view at 14:35 and 15:48 UT, respectively and appears to be moving linearly with a speed of about 300 km s^{-1}. It is a very faint CME and it is not observed in LASCO/C3. The first signatures of CME0.2 are very similar, with similar loop motions close
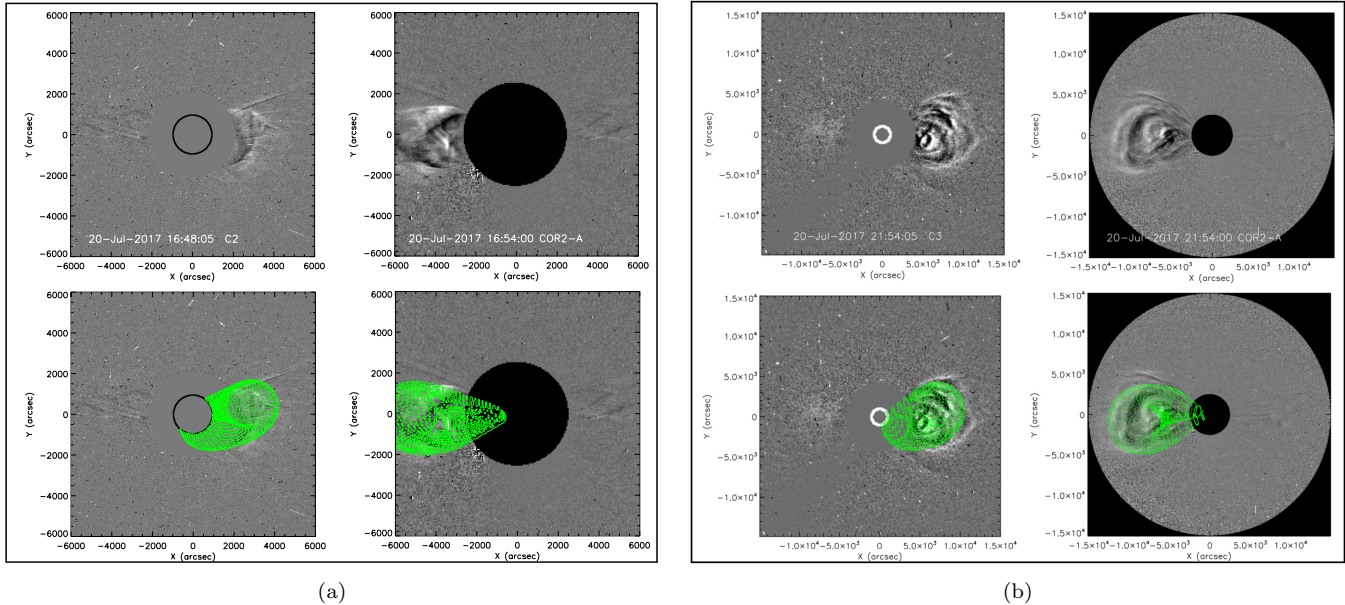
Figure 5. GCS reconstruction of two CMEs that erupted July 20 2017 and pre-condition the interplanetary space: a) a narrow, faint and slow CME0.1 directed between Mars and STEREO-B; b) a wider, brighter and faster CME0.2 directed towards STEREO-B. Parameters of the two CMEs are given in Table 2.

to the same AR as CME0.1, followed by a CME detection by COR1 at 17:50. The CME appears in the ST-A/COR2 at 19:10 UT, in LASCO/C2 at 18:24 UT, and in LASCO/C3 at 19:30 UT. CME0.2 decelerates in LASCO/C3 and has a highly distorted "wavy" leading edge, reaching a speed of around 600 km s^{-1}at approximately 20 R$_\odot$. The interaction of the two CMEs is very likely, but their main propagation direction is oriented more towards STEREO-B. Therefore, we conclude that the interplanetary space will not be affected by the two CMEs in the ST-A direction, but there might be some pre-conditioning in the Mars direction.

3.2. *CME propagation*

In Figure 6a a 2D representation of CME 1 and 2 widths and directions in the HEEQ[3] system is shown, as obtained from the GCS reconstruction. It can be seen that if we assume that the direction and the geometry do not change, CME1 is not expected to hit ST-A. Furthermore, CME1 *in situ* signatures at ST-A indicate lack of expansion, whereas at Mars there are expansion signatures, indicating CME2 is "pushing" CME1 much stronger in ST-A direction than in Mars direction, *i.e.* that the CME2 apex is directed closer to ST-A than Mars. As will be shown in the next section, the propagation/evolution modelling of the CMEs give reasonable results supporting that CMEs 1 and 2 are deflected towards ST-A by 15 and 20 degrees, respectively. We might consider CH2 (see Figure 4a) as a potential deflection source as it lies just east of the AR and deflection by 15-20 degrees would not be an unusual value given its proximity to CMEs source regions (see *e.g.* Gopalswamy et al. 2009). However, the deflection by CHs usually occurs at lower heights, within a couple solar radii, where we would expect to observe it already in coronagraphs (*e.g.* Kay et al. 2013) and therefore the deflection of CMEs 1 and 2 at heights > 15 R$_\odot$ due to CH2 is not likely. Another possible explanation is the deflection in the interplanetary space due to CME-CME interaction (Gopalswamy et al. 2001). CME1 might also be deflected due to interaction with CME2 similarly as it would be expected that slow CMEs are deflected towards west when moving in a fast solar wind (Wang et al. 2004, 2014), however, even considering that the momentum of CME1 is not negligible compared to CME2, this cannot easily explain the deflection of CME2. Finally, one should not forget on the limitations of the observational methods, where a 10° error in the CME direction is not unusual (Mierla et al. 2010). We also note that CME2 is a complex CME, which also might influence the determination of the direction. Based on these considerations as well as modelling attempts/efforts, for the purpose of analysis of CME

---

[3] Heliocentric Earth Equatorial

Table 2. CME parameters obtained from GCS reconstruction (a) and used for heliospheric propagation (b)

	CME1	CME2 (COR1)	CME2 (COR2)	CME0.1	CME0.2
a) GCS reconstruction parameters					
longitude (degrees)	170	185	190	150	117
latitude (degrees)	10	-7	-17	-5	-6
tilt (degrees)	-5	15	0	-25	-37
aspect ratio	0.35	0.5	0.9	0.27	0.35
half angle (degrees)	25	60	10	20	30
b) initial parameters for heliospheric propagation					
longitude (degrees)	-175	–	-150	150	117
latitude (degrees)	10	–	-10	-5	-6
half angle (degrees)	44	–	74	–	–
r_{min} (degrees)	23	–	22	20	23
r_{max} (degrees)	38	–	40	32	38
start date & time	2017-07-23 05:20	–	2017-07-23 06:00	2017-07-21 01:00	2017-07-21 02:30
speed (km s^{-1})	950	–	2700	300	600

propagation, evolution and their interaction we can assume that the directions of CMEs 1 and 2 in HEEQ system are changed with respect to the ones obtained by the GCS reconstruction (see Table 2 and Figure 6c).

Figure 6b shows the CME 1 and 2 early kinematics, as obtained by the GCS reconstruction. The measured kinematic curves of CME 1 and 2 apexes are given in a distance-time plot, where an error of 5% was assumed. It can be seen that measured 3D kinematics is in both cases represented well by motion with constant speeds of 950 km s^{-1} and 2700 km s^{-1}, respectively. To estimate the CME speed at the inner boundary for the propagation models used in sections 3.2.1 and 3.2.2 (20 R$_\odot$ and 21.5 R$_\odot$, respectively) we extrapolate GCS-obtained kinematics assuming constant speed.

The angular extent of CMEs 1 and 2 in the equatorial plane was estimated as: $\omega_{max} - (\omega_{max} - \omega_{min}) \times |tilt|/90$, where ω_{max} and ω_{min} are face-on and edge-on widths according to Thernisien (2011) and the tilt is the angle of the croissant axis with respect to the equatorial plane. This method was used previously to estimate the CME half-width with the assumed cone geometry by (Dumbović et al. 2018a; Guo et al. 2018a) and takes into account CME tilt, but not the latitude. Therefore, to cross-check the validity of this method we in addition estimate the CME opening angle using the ecliptic cut of the GCS-reconstructions[4], obtaining a similar result (within ±5°). For the purpose of simulating an elliptical cross section of the cone, which is needed for numerical simulations shown in Section 3.2.2, the method is adapted to calculate the major and minor axis obtaining $r_{min} = 23°$ and $r_{max} = 38°$ for CME1 and $r_{min} = 22°$ and $r_{max} = 40°$ for CME2. All initial CME parameters used as an input for propagation models, as well as GCS reconstruction parameters are given in Table 2. We note that GCS reconstruction was performed separately for COR1 and COR2, but for the purpose of heliospheric propagation COR2 reconstruction was used (see section 2.1 for details). CMEs 0.1 and 0.2 are included in Table 2 as their input was used for simulations in section 3.2.2.

3.2.1. *Drag-based model (DBM)*

We model the kinematics of CMEs 1 and 2 separately for ST-A and Mars directions using the drag-based model (DBM, Vršnak et al. 2013) adapted for the cone geometry (Žic et al. 2015). The initial CME parameters are based on the GCS reconstruction (see Table 2), whereas the parameters used to describe the effect of the ambient solar wind are taken to be different in the two directions. In ST-A direction we assume that there is no influence on the CME kinematics by previous 2 CMEs (CME0.1 and 0.2) and therefore assume the "standard" drag for CME1 ($\gamma = 0.2 \times 10^{-7}$ km^{-1}, see Vršnak et al. 2013, 2014). For CME2 we estimate a reduced drag ($\gamma = 0.1 \times 10^{-7}$ km^{-1}) caused by pre-conditioning of the IP space due to CME1. We use a "standard" solar wind speed for both CMEs in ST-A direction (400 km s^{-1}, see Vršnak et al. 2014; Dumbović et al. 2018b). The solar wind speed observed *in situ* before the arrival of the CMEs at ST-A is somewhat higher (500 km s^{-1}), however, we note that the ambient solar wind speed used by DBM corresponds to the solar wind CME moves through, and therefore does not necessarily

---

[4] this method takes into account both the latitude and the tilt, but the estimation is performed by the observer and is therefore somewhat subjective

correspond to the *in situ* speed measured before the ICME. On the other hand, the observed solar wind speed after the CME passage, which might be a better proxy for the ambient solar wind speed, is ~ 400 km s^{-1}.
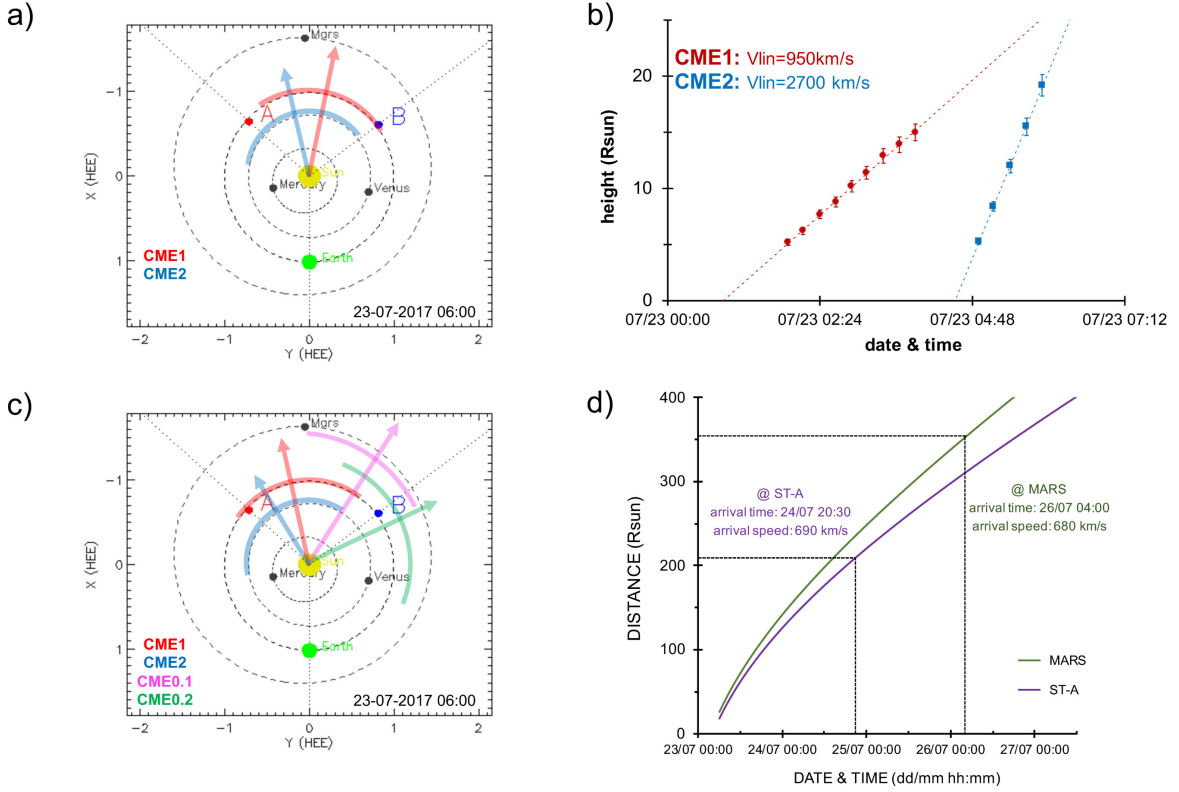

Figure 6. CME directions and kinematics obtained by GCS reconstruction and drag-based model (DBM): a) 2D representation of CMEs 1 and 2 halfwidths and directions in HEEQ system as obtained from GCS reconstruction (the red and blue arrows mark the IP direction of CMEs 1 and 2, respectively, whereas differently coloured arcs provide the angular extent of a corresponding CME); b) GCS-reconstructed kinematics of the CME1 and CME2 apexes; c) 2D representation of CMEs 0.1, 0.2, 1 and 2 halfwidths and directions in the HEEQ system as used in modelling (the red, blue, magenta, and green arrows mark the IP direction of CMEs 1, 2, 0.1 and 0.2, respectively, whereas differently coloured arcs provide the angular extent of a corresponding CME); d) DBM-obtained kinematics of the interacting CMEs (the merged CME1+2 structure) in ST-A and Mars direction.

In Mars direction we assume that the drag parameter for CME1 is lower than the "standard" value of $\gamma = 0.2 \times 10^{-7}$ km^{-1}, due to pre-conditioning by previous CMEs (CMEs 0.1 and 0.2) which "cleared the path", similar as Rollett et al. (2014). Based on the *in situ* observations by MAVEN and MSL/RAD, but also based on the GCS-related estimates of directions and angular extent of CMEs 0.1 and 0.2, we do not expect their interaction with CMEs 1 and 2 in the Mars direction. However, we find it likely that their propagation partly influences the ambient solar wind through which CMEs 1 and 2 propagate on their way to Mars. Therefore, we estimate a somewhat lowered drag for CME1 ($\gamma = 0.15 \times 10^{-7}$ km^{-1}) and reduced drag for CME2 ($\gamma = 0.1 \times 10^{-7}$ km^{-1}, as assumed for the ST-A direction). In Mars direction we initially use the same solar wind speed as in the ST-A direction, however we note that much better results are obtained with estimated speed of 500 km s^{-1}. We note that solar wind speed observed *in situ* before the arrival of the CMEs at Mars is somewhat lower (350 km s^{-1}), on the other hand the observed solar wind speed after the CME passage is ~ 600 km s^{-1}.

We model CMEs 1 and 2 separately and obtain their DBM kinematical curves for ST-A and Mars direction. For each direction we estimate the interaction point for the 2 CMEs based on the condition that the two kinematical curves cross each other. We note that physically this is highly idealised, because we implicitly assume that the CME is fully represented with an infinitesimally thin leading edge. Nevertheless, the procedure provides a quick and simple estimate of the interaction point, whereas any idealisations can be regarded as introducing an uncertainty in the timing. Similar procedure was used by Guo et al. (2018a), where the interaction point was derived based on the kinematical curves for the apexes of the corresponding CMEs assuming that all CME leading edge segments interact at the same time. Here

the angular separation of the CME apexes is too large and thus we allow that interaction of different segments can occur at different times. We find that the interaction occurs almost immediately after the CME 2 launch by DBM, at 18.2 $R_\odot$ and 26 $R_\odot$ in the ST-A and Mars direction, respectively.

We assume that the momentum is conserved during the interaction and that after the interaction the 2 CMEs continue to propagate as a merged entity, similar as Temmer et al. (2012) and Guo et al. (2018a). The direction of the merged entity is presumably defined by the direction of the faster CME (which 'drives" the whole entity), whereas the width is determined by the angular extent of the wider CME. The mass of the merged entity is given as the sum of masses of the two CMEs, where we assume that both CMEs have comparable masses. We note that this is a somewhat arbitrary mass estimation, because we do not actually measure the CME mass. On the other hand, we note that both CMEs are quite bright and interact very close to the Sun, therefore mass measurements might very likely have large uncertainties and moreover we are only interested in the mass *ratio*. With these assumptions, DBM can be recalculated for the merged entity, where the initial speed is given by the momentum conservation and the new drag parameter is re-calculated as $\gamma_{1+2} = \gamma_1 M_1 sin^2\omega_{1+2}/[(M_1 + M_2)sin^2\omega_1]$, where M_1 and M_2 are masses of CME 1 and 2, ω_1 and ω_{1+2} are half-widths of CME 1 and merged entity, and γ_1 is the drag-parameter of CME 1 (calculation based on equation 2 in Vršnak et al. 2013). Note that the re-calculated drag parameter is different in ST-A and Mars direction, as is the solar wind speed. The kinematic curves for the interacting CMEs are plotted in Figure 6d. The estimated arrival time at ST-A is July 24 at 20:30 UT with the arrival speed of 690 km s^{-1}, whereas the measured arrival time is July 24 23:00 UT with arrival speed of 660 km s^{-1}. The estimated arrival time at Mars is July 26 at 04:00 UT with the arrival speed of 680 km s^{-1}, whereas the measured arrival time is July 26 02:00 UT with arrival speed of 700 km s^{-1}.

In addition, we perform an ensemble run of the drag-based model (DBEM, Dumbović et al. 2018b), where the ensemble input is produced manually based on the standard DBM input as obtained from GCS reconstruction using the method described by Dumbović et al. (2018b). DBEM is not suitable to take into account CME-CME interaction, therefore, we regard only the merged entity as derived by DBM. We produce 48 CME ensemble members separately for ST-A and Mars directions for the merged entity based on the input used in DBM assuming error ranges of 1h for the start time, 200 km s^{-1} for the initial speed and 10° for longitude and width, whereas we use 15 synthetic values for solar wind speed and drag parameter assuming error ranges of 0.05 $\times 10^{-7}$ km^{-1} and 50 km s^{-1}, respectively. In ST-A direction DBEM predicts a 100% arrival probability with likeliest arrival time (median) at July 24 21:30 UT and a spread of ±4.5h, whereas the likeliest arrival speed is 690 km s^{-1} with a spread of −80 km s^{-1}/+110 km s^{-1}. In Mars direction DBEM also predicts 100% arrival probability with likeliest arrival time (median) at July 26 06:00 UT and a spread of −7.5h/+7h, whereas the likeliest arrival speed is 670 km s^{-1} with a spread of −60 km s^{-1}/+80 km s^{-1}. In both cases the observed arrival times and speeds are within the predicted spread. Given the usual forecast errors for CME propagation (*e.g.* Dumbović et al. 2018b; Wold et al. 2018; Riley et al. 2018, and references therein) this is a reasonable agreement with the observations. Therefore, based on the DBM/DBEM results we conclude that it is highly likely that both CMEs interact close to the Sun, arrive "together" at ST-A and Mars and that the ambient solar wind through which CMEs propagate is different in the ST-A and Mars direction. There are indications that two previous CMEs pre-condition the IP space in the Mars direction lowering the drag, and moreover, that in the Mars direction CMEs propagate through higher-speed solar wind than in ST-A direction.

3.2.2. *WSA-ENLIL+Cone simulation*

We perform a WSA-ENLIL+Cone heliospheric simulation (Odstrcil 2003; Odstrcil et al. 2004, 2005) which is available through the *Runs-on-Request* system of the Community Coordinated Modeling Center (CCMC[5]). The runs consider not only the merging CMEs 1 and 2, but also the pre-conditioning CMEs 0.1 and 0.2 and are based on the initial parameters given in Table 2. They are based on NSO/GONG magnetogram synoptic maps with a boundary condition type of time-independent single daily update. We note that there is an existing run published by Luhmann et al. (2018), however since the focus of their study are SEPs, they do not consider CMEs 0.1 and 0.2. The input is based on GCS, similar as for DBM, adapted for ENLIL (cone elliptical cross section). The simulation is available at https://ccmc.gsfc.nasa.gov/database_SH/Manuela_Temmer_112618_SH_1.php.

The simulation reveals that CMEs 0.1 and 0.2 already merge close to the Sun and practically move as one entity, which is a bit slower in the Mars direction compared to STEREO-B and does not arrive at STEREO-A. CMEs 1
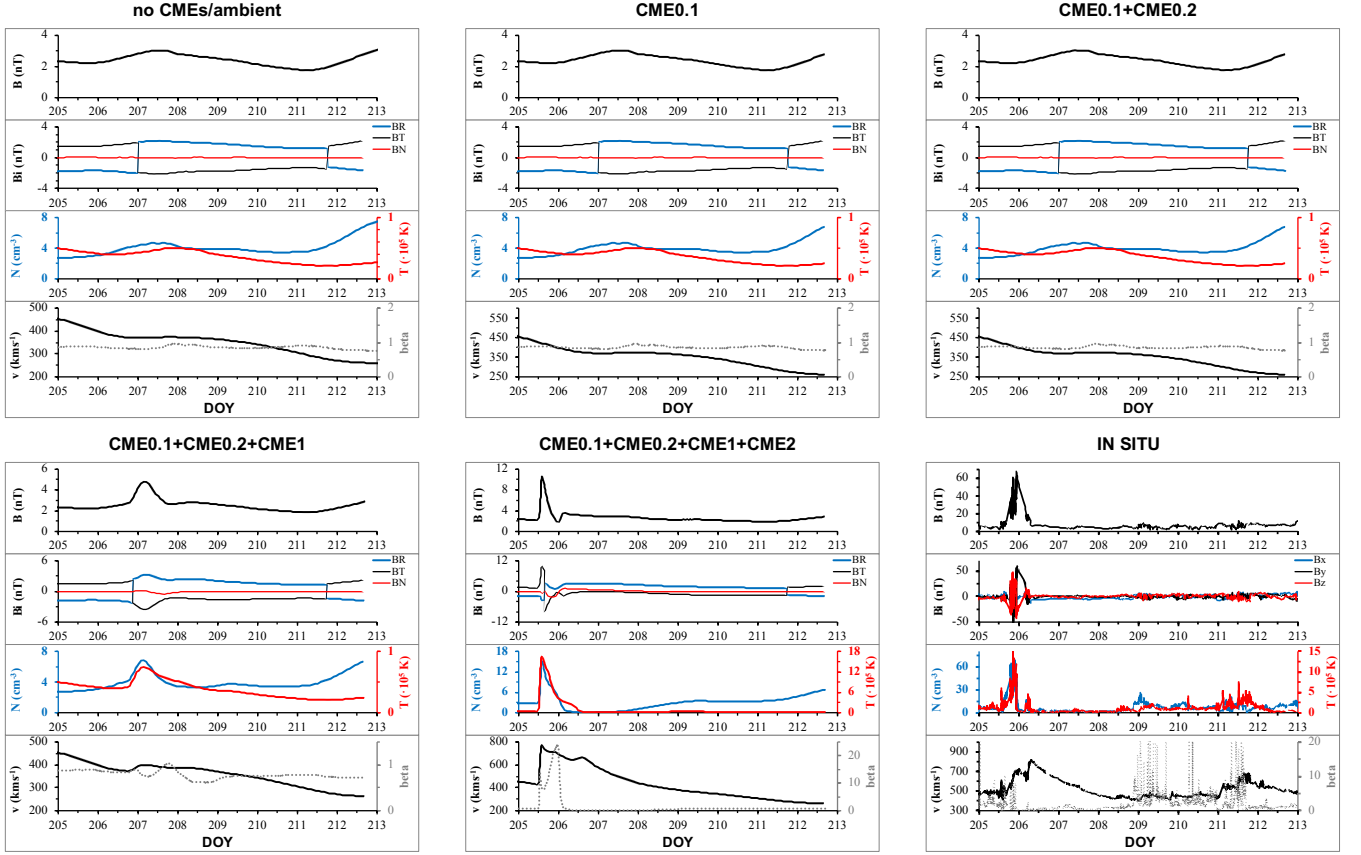
---

[5] https://ccmc.gsfc.nasa.gov/requests/requests.php

Figure 7. ENLIL multiple block-run results for ST-A for quiet-time ambient (without any CMEs, top left panels), inclusion of CME0.1 (top middle panels), inclusion of CMEs 0.1 and 0.2 (top right panels), inclusion of CMEs 0.1, 0.2 and 1 (bottom left panels), a full suite run with CMEs 0.1, 0.2, 1 and 2 (bottom middle panels) and *in situ* measurements by ST-A/PLASTIC (bottom right panels). The panels in each block correspond to (top to bottom) 1-total magnetic field strength, 2-magnetic field strength of three components of the magnetic field, 3-plasma density and temperature, and 4-plasma velocity and beta parameter. The magnetic field components of the ENLIL runs correspond to the RTN coordinates of the HEEQ system, whereas for the ST-A they correspond to RTN coordinates with radial component defined by the Sun-spacecraft line. *(DOY=day of year 2017)*

and 2 also merge quite close to the Sun and "pick-up" CMEs 0.1 and 0.2 in the Mars direction. However, it can be seen that the fastest part of the merged CME1+2 entity is directed towards STEREO-A and not Mars, probably due to the longitudinal direction of much faster CME 2 (150°). The predicted arrival time of the disturbance at ST-A is July 24 around 12:00 UT, which fits very good with observation (July 24 around 13:00 UT, see region 1 in Figure 3-left). The predicted arrival time of the disturbance at Mars is July 26 around 15:00 UT, which is almost 1 day later than the observed shock arrival (July 25 around 17:00 UT, see region 2 in Figure 3-right). In addition, we perform an ENLIL ensemble run (Mays et al. 2015), where the ensemble input is produced manually based on the standard ENLIL input as obtained from GCS reconstruction using the method described by Dumbović et al. (2018b). The input is slightly different than that for DBEM, because for DBEM we produced a unique ensemble based on the merged entity parameters, whereas for ENLIL we produce ensemble input (24 ensemble members) for each of the 4 CMEs separately. The full input and the results of the run are available at https://iswa.gsfc.nasa.gov/ENSEMBLE/ 2017-07-20_ncmes4_sims23_HILOX069/. In ST-A direction the simulation predicts a 100% arrival probability with median input arrival time at July 24 10:30 UT, average arrival at July 24 11:20 UT and a spread of −6h/+18.5h. In Mars direction the simulation predicts only 61% arrival probability with median input arrival time at July 26 06:00 UT, average arrival at July 26 02:00 UT, and a spread of −14h/+6.5h, *i.e.* the observed arrival time is within the predicted spread. We note that the low hit probability is most likely related to the underestimated longitudinal spread. It is important to highlight that we used CME (magnetic structure) input for the simulations, whereas ENLIL simulates the evolution/propagation of the density disturbance and is therefore more suitable for simulation of the shock. The
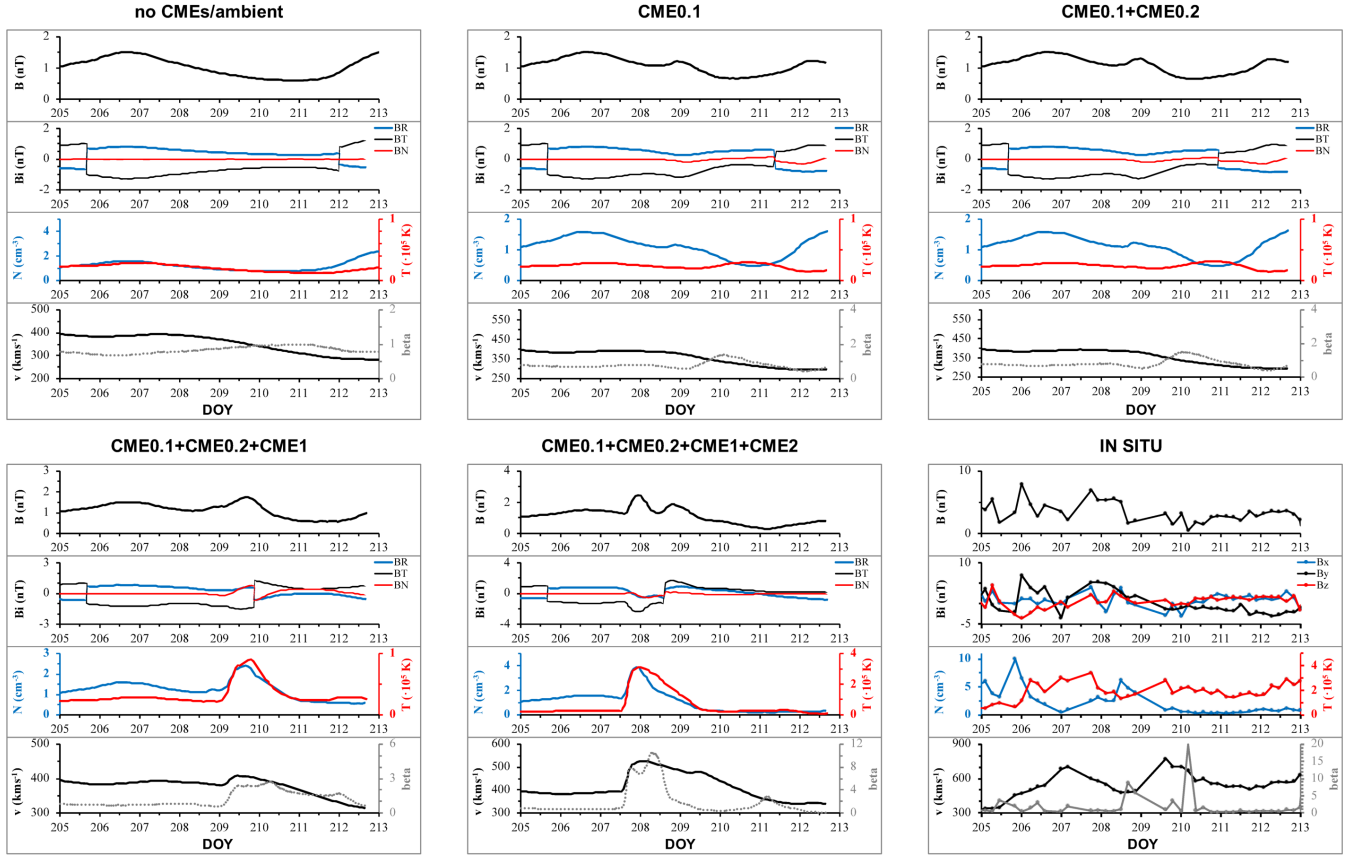
Figure 8. ENLIL multiple block-run results for Mars for quiet-time ambient (without any CMEs, top left panels), inclusion of CME0.1 (top middle panels), inclusion of CMEs 0.1 and 0.2 (top right panels), inclusion of CMEs 0.1, 0.2 and 1 (bottom left panels), a full suite run with CMEs 0.1, 0.2, 1 and 2 (bottom middle panels) and *in situ* measurements by MAVEN (bottom right panels). The panels in each block correspond to (top to bottom) 1-total magnetic field strength, 2-magnetic field strength of three components of the magnetic field, 3-plasma density and temperature, and 4-plasma velocity and beta parameter. The magnetic field components of the ENLIL runs correspond to the RTN coordinates of the HEEQ system, whereas for MAVEN they correspond to RTN coordinates of the MSO system, with the radial component defined by the Sun-Mars line.*(DOY=day of year 2017)*

shock can have a larger spatial extent than the magnetic structure of CME 2, can be driven closer to the Mars direction and not significantly influenced by July 20 CMEs. However, in our study we are more interested in the qualitative description of the CME 1 and 2 interaction, than accurate CME 2 shock propagation, therefore we do not attempt to obtain a better arrival time match by introducing the shock-related input.

For a better qualitative analysis of the events observed at ST-A and Mars we use the ENLIL multiple block runs. The multiple block runs allow us to see how the simulation results change by consecutively adding CMEs in the simulation. The first run describes the ambient medium, without any CMEs, the second run includes the first CME of July 20 (marked as CME0.1), the third run includes both the first (CME0.1), as well as the second CME of July 20 (marked CME0.2), the fourth run includes both CMEs of July 20 and CME1, and finally the last run includes all four CMEs. The performed multiple block runs are available as separate synthetic *in situ* profiles at different targets in the output files of the simulation. In Figures 7 and 8 ENLIL multiple block run results are shown for heliospheric positions corresponding to ST-A and Mars, respectively. From top-left to bottom-right different panels show runs starting from no CMEs to inclusion of all 4 CMEs (as described above), where the last panel shows *in situ* measurements on the same time scale.

Two sector boundaries are observed in the multiple block-run plots in Figure 7. The first one corresponds to the SIR originating from the CH observed to pass the central meridian (as seen from Earth) around July 5 and very likely corresponds to CH1 analysed in Section 3.1. The second one corresponds to the SIR originating from the CH eastward of the AR from which CME 1 and 2 originate, which is observed to pass the central meridian (as seen from
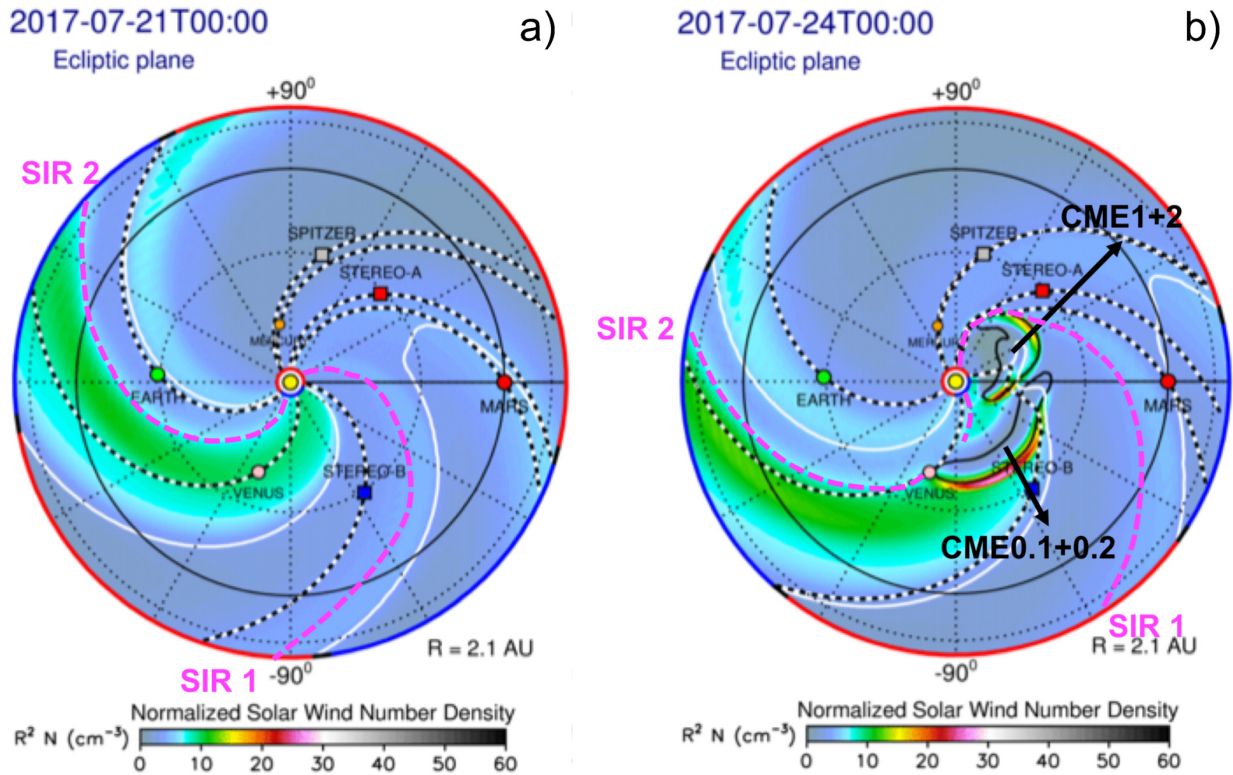
Figure 9. Selected timeframes of the ENLIL simulation: quiet time (a) and propagation phase (b), where first propagating disturbance represents merged CME0.1 and 0.2 entity (CME0.1+0.2) and the second merged CME 1 and 2 entity (CME1+2). SIR1 and SIR2 are approximatively highlighted at the density change by a magenta dashed line. SIR2 is disconnected before and after the CMEs in (b).

Earth) around July 13 and very likely corresponds to the CH2 analysed in Section 3.1. It can be seen that inclusion of 2 CMEs that preceded CMEs 1 and 2 do not impact the *in situ* observations at ST-A. Furthermore, it can be seen that in a full suite run (CME0.1+CME0.2+CME1+CME2) there is a qualitative agreement with the observed *in situ* double-CME signatures. Moreover, the simulation indicates that SIR1 is "squeezed" in the sheath region of CMEs 1 and 2. Although this cannot be confirmed by *in situ* measurements due to the data gap, we note that we do not find SIR1 signatures in front of CMEs 1 and 2. We also note that the complete lack of an expanding profile of CME1 also indicates there might be a structure in front of it, inhibiting its expansion, with SIR1 being the only candidate to explain this. Therefore, we argue that it is indeed possible that the SIR1 is "squeezed" in the sheath region of CMEs 1 and 2, as the simulation indicates. The timing of the second sector boundary roughly corresponds to the observed SIR signatures between DOY 211 and 212, likely originating from CH2.

In Figure 8 again two sector boundaries can be observed in the ENLIL multiple block runs, corresponding to the same CH as the ones observed in Figure 7. However, it can be seen that in the Mars direction the first SIR reaches Mars before it interacts with CMEs 1 and 2 and roughly corresponds with the timing of the SIR signatures observed in region 1 in Figure 3. On the other hand, according to the simulation SIR2 is strongly affected by CMEs. It can be seen that inclusion of CME0.1 and CME0.2 impacts *in situ* observations at Mars, but their signatures are entirely lost in a full suite run. This indicates that CME0.1 and CME0.2 affect the ambient solar wind, but we would not expect to see their significant impact at Mars. Furthermore, in a full suite run we observe SIR2 being "squeezed" between CMEs 1 and 2, which seems to be in contradiction with the fact that CH2 is trailing the AR and that the two CMEs merge already in the corona. While this might be an artefact related to the fact that ENLIL runs do not involve magnetic structures (CMEs are introduced as pressure pulses), it is important to note that the SIR signatures are indeed observed in the MAVEN data between the two CMEs, with the timing roughly corresponding to SIR2 from simulations. A possible explanation is that an interchange reconnection occurs between the open field lines of CH2 and the leg of CME1 (similar as described by Crooker et al. 2002). This might result in open field lines of both CME1 and the nearby CH2 (see the northern part of CH2 in Figure 4b) being caught between CMEs 1 and 2 producing SIR-like

signatures between the two CMEs. This would lead to SIR-like signatures observed at Mars, but also at ST-A, where we indeed do find SIR signatures. However, the latter is not expected from the ENLIL simulation.

We want to emphasise that the quantitative correspondence between synthetic *in situ* measurements of the ENLIL multiple block runs and real *in situ* measurements by MAVEN and ST-A is quite poor (*e.g.* magnetic field at ST-A is 4 times weaker in the simulation). On the other hand, we find that the multiple block runs in synergy with the *in situ* measurements are very insightful in understanding the "chronological" order of sub-structures observed *in situ* .

3.3. *CME evolutionary properties*

In order to analyse how CME1 evolves, *i.e.* how the size and the magnetic field change with heliospheric distance, we compare the initial FR properties (obtained from GCS) with *in situ* -measured properties at ST-A and Mars. For that purpose, we estimate the initial radius of the flux rope based on the last time step of the performed GCS reconstruction, which is taken as the initial time of the FR evolution. The radius of the FR obtained from the GCS reconstruction is different across the FR - it is largest at the apex and smallest at the flanks. Based on the direction of CME1 and the relative positions of the spacecraft, as the starting radius in the Mars direction we take the apex radius and in the ST-A direction we take the flank radius and we assume a 5% error (see Table 3). Based on the start time and the observed *in situ* arrival time we calculate the transit time to ST-A and Mars and assume ±1h error. The final radius of the FR at ST-A was obtained based on the FR orientation and impact parameter obtained from the Lundquist fitting (Lundquist 1951; Leitner et al. 2007), according to the method described by Vršnak et al. (2019). At Mars we estimate the radius assuming that the spacecraft passes the FR vertically with respect to the FR axis using the expanding profile of plasma flow speed. The error of the radius is determined *via* error propagation assuming SW speed and FR duration errors of 5%. The central axial field strength at ST-A is obtained from the Lundquist fitting, whereas at Mars we estimate it based on *in situ* measurements assuming it corresponds to the maximum measured value (note that there is a data gap at the start of the ICME, therefore, the maximum is around ICME center). In both cases we assume an error of 1 nT, which is around 15% for Mars, but we note that due to the MAVEN data gap at the front of the CME it is reasonable to assume larger error. Using these *in situ* values we calculate the axial magnetic flux of the flux rope using equation 52 from DeVore (2000) derived for Lundquist-solution FR, $\Phi_{\mathrm{FIN}} = 1.4B_{\mathrm{c,FIN}}a_{\mathrm{FIN}}^2$, where B_c is the central axial field strength. The obtained flux values at Mars and ST-A are different (see Table 3), indicating different evolution in two different directions of propagation. Note that the result shown in Table 3 is closely related to the assumption of the Lundquist solution, whereas considering different sets of assumptions might yield that the factor of 2 difference in the flux is not significant.

Assuming that the FR radius a is expanding self-similarly following a power-law, $a = a_0(R/R_0)^{n_a}$ (see *e.g.* Démoulin et al. 2008; Gulisano et al. 2012; Vršnak et al. 2019) the power-law index n_a can be derived using the initial and final distance/FR radius. We note that $n_a = 1$ indicates an isotropic self-similar expansion, whereas $n_a < 1$ and $n_a > 1$ could indicate a weaker or stronger expansion, respectively, as the observational studies roughly constrain n_a to $0.45 < n_a < 1.14$ (*e.g.* Bothmer and Schwenn 1998; Leitner et al. 2007; Gulisano et al. 2012; Vršnak et al. 2019). Using the values presented in Table 3 we calculate the power-law index n_a in ST-A and Mars direction separately, allowing that the FR expands differently in two different directions. The errors are calculated by estimating the upper and lower power-law curves based on the error bars of the datapoints (for a more detailed description see Vršnak et al. 2019). We observe that n_a is much smaller in ST-A direction than Mars direction, indicating that radial expansion is much weaker in the ST-A direction, in agreement with *in situ* observation.

Self-similar expansion of the FR is also related to the drop in the magnetic field, which can also be described *via* power-law, $B = B_0(R/R_0)^{-n_B}$ (see *e.g.* Démoulin et al. 2008; Gulisano et al. 2012; Vršnak et al. 2019). We note that $n_B = 2$ indicates an isotropic self-similar expansion, but observations constrain it to $0.84 < n_B < 2.19$ (*e.g.* Gulisano et al. 2012; Vršnak et al. 2019, and references therein). Deriving the power-law index n_B is not trivial, because we do not know the initial central magnetic field strength. For that purpose, we use the *ForbMod* model (Dumbović et al. 2018a) which describes interaction of galactic cosmic rays (GCRs) and a flux rope during its propagation and evolution in the heliosphere. The model assumes that the FR is initially empty of GCRs, that it expands self-similarly and fills-up slowly with GCRs which diffuse into it. As a result, after a certain time the FR will be partly filled with particles and consequently GCR observation will show a drop during the FR passage, *i.e.* a Forbush decrease. The FD amplitude at a specific heliospheric distance therefore depends on the expansion rate of the FR and the diffusion rate (*i.e.* diffusion coefficient) and is given by an analytical expression (for a detailed description of the model see Dumbović et al. 2018a). Using the measured FD amplitude and with several simple assumptions we can use the

Table 3. Flux rope initial (GCS), *in situ* and evolutionary characteristics

	ST-A	Mars
start time	2017-07-23 03:54 UT	2017-07-23 03:54 UT
start height, R_0	15 $R_\odot$	15 $R_\odot$
GCS radius, a_0	(2.8 ± 0.1) $R_\odot$	(3.9 ± 0.2) $R_\odot$
final distance, $R(t)$	208 $R_\odot$	352 $R_\odot$
transit time	(43 ± 1) h	(70 ± 1) h
in situ radius, a_{FIN}	(13 ± 2) $R_\odot$	(48 ± 5) $R_\odot$
in situ central magnetic field strength, $B_{\mathrm{c,FIN}}$	(40 ± 1) nT	(7 ± 1) nT
in situ magnetic flux, Φ_{FIN}	$(5 \pm 1) \cdot 10^{20}$ Mx	$(1.1 \pm 0.3) \cdot 10^{21}$ Mx
power-law radius expansion index, n_a	$0.58^{+0.07}_{-0.08}$	0.80 ± 0.05
FD magnitude	$-$	$(2.8 \pm 0.2)\%$
power-law magnetic field expansion index, n_B	~ 1.8	~ 2.1
expansion type, $x = n_B - 2n_a$	$x > 0$	$x > 0$
initial central magnetic field strength, B_0	~ 0.05G	~ 0.05G
initial axial flux, Φ_0	$\sim 5 \cdot 10^{21}$ Mx	$\sim 5 \cdot 10^{21}$ Mx

Note—B_0 and Φ_0 were modelled based on cosmic ray data and are assumed to be the same for both directions (for a detailed explanation on the calculation see main text).

model to estimate the initial central magnetic field strength. Firstly, we assume that the observed FD amplitude can be associated with particles of a relatively narrow specific energy range, *i.e.* that MSL/RAD is mostly sensitive to particles of certain energy. We note that this a somewhat arbitrary assumption, because MSL/RAD measurements have contributions from different particles, *i.e.* radiation sources, including both primary and secondary GCRs, electrons, etc. Nevertheless, MSL/RAD measurements were found to be a very useful proxy for GCRs, especially regarding FD measurements (Guo et al. 2018b). The Martian atmosphere shields away lower-energy GCRs (< 150 MeV, *i.e.* 0.55 GV) and modifies incoming GCR spectra so that higher-energy particles are less modulated (Guo et al. 2018b). On the other hand, the interplanetary GCR spectrum drops very fast with rigidities above 1 GV, thus it is reasonable to assume that MSL/RAD is mostly sensitive to particles around a certain energy. We use a particle transport model, the Atmospheric Radiation Interaction Simulator (AtRIS, Banjac et al. 2019), which was validated for MSL/RAD by Guo et al. (2019), and estimate that MSL/RAD is mostly sensitive to particles of rigidity ~ 2.5GV. Secondly, we assume that the expression for the diffusion coefficient is governed by the power-law behaviour due to its relation to the magnetic field (*i.e.* $D \sim 1/B$) and that it is scaled to the radial perpendicular diffusion coefficient at Earth as given in Potgieter (2013). With these assumptions and fitting the model to observations (see Figure 3-right) it is possible to estimate n_B in the Mars direction (see equation 1 in Rodari et al. 2019) and therefore make an order of magnitude estimation of the initial FR central magnetic field strength and flux.

We find that the magnetic field inside the FR drops faster in the Mars direction than ST-A direction, which is in agreement with *in situ* observations, where the magnetic field at ST-A is unusually strong compared to MAVEN. Namely, if we calculate the power-law index of the magnetic field drop, $B = B_0(R/R_0)^{-n_B}$, using B_0, R_0 and B, R for ST-A and Mars, respectively, $n_B = 3.3$ is obtained, which is much higher than observationally constrained values, indicating that the magnetic field drop rate is in fact different in the ST-A and Mars directions, as obtained from the *ForbMod* calculation.

Based on the self-similar expansion expressions and considering a Lundquist-type solution with a circular cross-section, it can be seen that the axial magnetic flux rope can also be expressed by a power-law as $\Phi = \Phi_0(R/R_0)^{-x}$, where $x = n_B - 2n_a$ denotes an expansion type (for $x = 0$ the flux is conserved, for $x < 0$ increased for $x > 0$ decreased, see Dumbović et al. 2018a). Based on these considerations we find that both in the ST-A and Mars direction $x > 0$ indicating that the axial flux of the FR is effectively reduced, possibly through erosion due to interaction. Assuming that the initial flux is the same in both directions, our results suggest that the axial flux might be reduced more efficiently in the ST-A direction than Mars direction (Table 3), however, we note that the uncertainties are too large to make a more reliable conclusion.

4. DISCUSSION AND CONCLUSION

We study the solar and interplanetary sources of one of the biggest FDs observed at Mars on July 24 2017. The analysis of *in situ* observations at ST-A and Mars presented in Sections 2.2 and 2.3 indicates that regions 3/yellow and 5/red in Figure 3 correspond to two ICMEs, most likely CME1 and 2. Both at ST-A and Mars shock/sheath signatures are observed, however in ST-A direction there is a data gap in the shock/sheath region which hampers a reliable and uniqe interpretation of the *in situ* signatures within this region. Both at ST-A and Mars an interaction region is observed between the two CMEs (region 4/orange in Figure 3), however the interaction region is much longer/broader at Mars compared to ST-A. Finally, at Mars a HSS signature is observed at the back of the second ICME (region 6/green in Figure3), whereas such region is not observed in ST-A. Combining the DBM results with the *in situ* signatures described in Sections 2.2 and 2.3 there are strong indications that regions 3/yellow and 5/red in Figure 3 correspond to CME1 and CME2 at ST-A and Mars, respectively. In addition, we do not observe *in situ* signatures of CMEs 0.1 or 0.2 at ST-A or Mars. Finally, we note that region 6 in Figure 3 (with high-speed stream signatures) supports the DBM result of CMEs propagating through higher-speed solar wind in the Mars direction.

The ENLIL simulations are in agreement with the DBM results and *in situ* interpretations of CMEs 1 and 2 corresponding to regions 3 and 5 at ST-A and Mars, respectively. Moreover, the simulations indicate that SIR1 is "squeezed" in front of CME1 in the ST-A direction, which might be in agreement with a very intense second part of the shock/sheath (region 2/blue) observed in Figure 3. However, due to the data gap in the *in situ* measurements this cannot be confirmed. On the other hand, in Mars direction SIR1 arrives shortly before CME1, corresponding to the stream interface signatures and a first decrease in RAD data observed in region 1/green in Figure 3.

The most likely source of SIR1 is a CH passing the central meridian of ST-A at the day of eruption (CH1, see Figure 4a). The simulation is also in agreement with the expansion profiles observed *in situ* at ST-A and Mars. In the ST-A direction CME1 is, according to the simulation, constrained between CME2 and SIR1 and thus should not expand notably, as is indeed observed. In the Mars direction on the other hand, both the simulations and *in situ* measurements indicate that SIR1 is not "pushed" by CME1. Therefore, we might expect CME1 to expand more freely in the Mars direction, in agreement with the expanding profile observed in the *in situ* measurements. The analysis of the CME evolutionary properties further support the interpretation that the expansion of CME1 is hindered in ST-A direction, whereas it expands more freely in the Mars direction.

The most likely source of SIR2 is a horseshoe-shaped CH lying just next to the active region where CMEs 1 and 2 originate (CH2, see Figure 4b). The simulation shows how CMEs 1 and 2 "disconnect" SIR2 which partly becomes trapped between CMEs 1 and 2, whereas the HSS continues to stream out from CH2, propagating behind the two interacting CMEs in the ST-A direction. These simulation results are probably related to the fact that the simulations do not involve magnetic structures, on the other hand they do agree with the *in situ* measurements showing SIR signatures between two CMEs both at ST-A and Mars. These specific CME-SIR-CME signatures could be related to the interchange reconnection (*e.g.* Crooker et al. 2002) of the CME1 leg with a a nearby CH2, where the open field lines get "squeezed" between CMEs 1 and 2, whereas the majority of the HSS originating from CH2 propagates/corotates behind the CME2, lagging significantly behind CMEs in ST-A direction, but not in the Mars direction.

Finally, we might consider the possible consequences such an extreme space weather event might have had if it was Earth-oriented. In Figure 3 a very strong south-oriented B_z can be seen at ST-A, which could have produced a serious geomagnetic storm at Earth. Liu et al. (2019) calculated it would cause a severe geomagnetic storm with a Disturbance storm time index $Dst < -300$nT. We note that Liu et al. (2019) offered an alternative interpretation of the solar sources of the IP signatures observed by ST-A and Mars. They, however, also stress the complexity of the event, as well as preconditioning.

To summarise: based on the presented analysis which combines multi-instrument and multi-spacecraft measurements, as well as different modelling approaches, we find that peculiar *in situ* signatures at ST-A and Mars can be explained by CME-CME and CME-SIR interactions. In ST-A direction the interaction inhibited the expansion of the first CME thus resulting in magnetic cloud signatures with an extremely high magnetic field strength and of extremely short-duration. On the other hand, in the Mars direction CME-CME interaction accompanied by interaction with the ambient interplanetary plasma resulted in a complex, long-duration IP disturbance with many substructures, each of which added to the multi-step Forbush decrease, thus producing one of the biggest FDs ever detected on Mars. We underline that there is a highly speculative aspect of the proposed scenario as it is based on the methods and models suffering from significant uncertainties. Hence, other scenarios explaining this complex event might also be considered. However, we note that despite the uncertainties, different methods and models used in this study overlap in the proposed scenario, making it the most plausible explanation of the complex events.

REFERENCES

M. H. Acuña, D. Curtis, J. L. Scheifele, C. T. Russell, P. Schroeder, A. Szabo, and J. G. Luhmann. The STEREO/IMPACT Magnetic Field Experiment. *Space Sci. Rev.*, 136:203–226, April 2008. https://doi.org/10.1007/s11214-007-9259-2.

S. Banjac, K. Herbst, and B. Heber. The Atmospheric Radiation Interaction Simulator (AtRIS): Description and Validation. *J. Geophys. Res.*, 124:50–67, January 2019. https://doi.org/10.1029/2018JA026042.

A. V. Belov. Forbush effects and their connection with solar, interplanetary and geomagnetic phenomena. In N. Gopalswamy and D. F. Webb, editors, *IAU Symp.*, volume 257 of *IAU Symp.*, pages 439–450, March 2009. https://doi.org/10.1017/S1743921309029676.

V. Bothmer and R. Schwenn. The structure and origin of magnetic clouds in the solar wind. *Ann. Geophys.*, 16: 1–24, January 1998. https://doi.org/10.1007/s00585-997-0001-x.

G. E. Brueckner, R. A. Howard, M. J. Koomen, C. M. Korendyke, D. J. Michels, J. D. Moses, D. G. Socker, K. P. Dere, P. L. Lamy, A. Llebaria, M. V. Bout, R. Schwenn, G. M. Simnett, D. K. Bedford, and C. J. Eyles. The Large Angle Spectroscopic Coronagraph (LASCO). *Sol. Phys.*, 162:357–402, December 1995. https://doi.org/10.1007/BF00733434.

L. Burlaga, E. Sittler, F. Mariani, and R. Schwenn. Magnetic loop behind an interplanetary shock - Voyager, Helios, and IMP 8 observations. *J. Geophys. Res.*, 86: 6673–6684, August 1981. https://doi.org/10.1029/JA086iA08p06673.

L. Burlaga, D. Berdichevsky, N. Gopalswamy, R. Lepping, and T. Zurbuchen. Merged interaction regions at 1 AU. *J. Geophys. Res.*, 108:1425, December 2003. https://doi.org/10.1029/2003JA010088.

H. V. Cane. Coronal Mass Ejections and Forbush Decreases. *Space Sci. Rev.*, 93:55–77, July 2000. https://doi.org/10.1023/A:1026532125747.

H. V. Cane, I. G. Richardson, and T. T. von Rosenvinge. Cosmic ray decreases: 1964-1994. *J. Geophys. Res.*, 101: 21561–21572, October 1996. https://doi.org/10.1029/96JA01964.

N. U. Crooker, J. T. Gosling, and S. W. Kahler. Reducing heliospheric magnetic flux from coronal mass ejections without disconnection. *J. Geophys. Res.*, 107:1028, February 2002. https://doi.org/10.1029/2001JA000236.

P. Démoulin, M. S. Nakwacki, S. Dasso, and C. H. Mandrini. Expected in Situ Velocities from a Hierarchical Model for Expanding Interplanetary Coronal Mass Ejections. *Sol. Phys.*, 250:347–374, August 2008. https://doi.org/10.1007/s11207-008-9221-9.

C. R. DeVore. Magnetic Helicity Generation by Solar Differential Rotation. *Astrophys. J.*, 539:944–953, August 2000. https://doi.org/10.1086/309274.

M. Dumbović, B. Vršnak, J. Čalogović, and M. Karlica. Cosmic ray modulation by solar wind disturbances. *Astron. Astrophys.*, 531:A91+, July 2011. https://doi.org/10.1051/0004-6361/201016006.

M. Dumbović, B. Vršnak, and J. Čalogović. Forbush Decrease Prediction Based on Remote Solar Observations. *Sol. Phys.*, 291:285–302, January 2016. https://doi.org/10.1007/s11207-015-0819-4.

M. Dumbović, B. Heber, B. Vršnak, M. Temmer, and A. Kirin. An Analytical Diffusion-Expansion Model for Forbush Decreases Caused by Flux Ropes. *Astrophys. J.*, 860:71, June 2018a. https://doi.org/10.3847/1538-4357/aac2de.

M. Dumbović, J. Čalogović, B. Vršnak, M. Temmer, M. L. Mays, A. Veronig, and I. Piantschitsch. The Drag-based Ensemble Model (DBEM) for Coronal Mass Ejection Propagation. *Astrophys. J.*, 854:180, February 2018b. https://doi.org/10.3847/1538-4357/aaaa66.

C. J. Farrugia, V. K. Jordanova, M. F. Thomsen, G. Lu, S. W. H. Cowley, and K. W. Ogilvie. A two-ejecta event associated with a two-step geomagnetic storm. *J. Geophys. Res.*, 111(A10):A11104, November 2006a. https://doi.org/10.1029/2006JA011893.

C. J. Farrugia, H. Matsui, H. Kucharek, V. K. Jordanova, R. B. Torbert, K. W. Ogilvie, D. B. Berdichevsky, C. W. Smith, and R. Skoug. Survey of intense Sun Earth connection events (1995 2003). *Adv. Space Res.*, 38: 498–502, January 2006b. https://doi.org/10.1016/j.asr.2005.05.051.

S. E. Forbush. On the effects in cosmic-ray intensity observed during the recent magnetic storm. *Phys. Rev.*, 51(12):1108–1109, Jun 1937. https://doi.org/10.1103/PhysRev.51.1108.3.

J. L. Freiherr von Forstner, J. Guo, R. F. Wimmer-Schweingruber, D. M. Hassler, M. Temmer, M. Dumbović, L. K. Jian, J. K. Appel, J. Čalogović, B. Ehresmann, B. Heber, H. Lohf, A. Posner, C. T. Steigies, B. Vršnak, and C. J. Zeitlin. Using Forbush Decreases to Derive the Transit Time of ICMEs Propagating from 1 AU to Mars. *J. Geophys. Res.*, 123: 39–56, January 2018. https://doi.org/10.1002/2017JA024700.

A. B. Galvin, L. M. Kistler, M. A. Popecki, C. J. Farrugia, K. D. C. Simunac, L. Ellis, E. Möbius, M. A. Lee, M. Boehm, J. Carroll, A. Crawshaw, M. Conti, P. Demaine, S. Ellis, J. A. Gaidos, J. Googins, M. Granoff, A. Gustafson, D. Heirtzler, B. King, U. Knauss, J. Levasseur, S. Longworth, K. Singer, S. Turco, P. Vachon, M. Vosbury, M. Widholm, L. M. Blush, R. Karrer, P. Bochsler, H. Daoudi, A. Etter, J. Fischer, J. Jost, A. Opitz, M. Sigrist, P. Wurz, B. Klecker, M. Ertl, E. Seidenschwang, R. F. Wimmer-Schweingruber, M. Koeten, B. Thompson, and D. Steinfeld. The Plasma and Suprathermal Ion Composition (PLASTIC) Investigation on the STEREO Observatories. *Space Sci. Rev.*, 136:437–486, April 2008. https://doi.org/10.1007/s11214-007-9296-x.

N. Gopalswamy, S. Yashiro, M. L. Kaiser, R. A. Howard, and J.-L. Bougeret. Characteristics of coronal mass ejections associated with long-wavelength type II radio bursts. *J. Geophys. Res.*, 106:29219–29230, December 2001. https://doi.org/10.1029/2001JA000234.

N. Gopalswamy, P. Mäkelä, H. Xie, S. Akiyama, and S. Yashiro. CME interactions with coronal holes and their interplanetary consequences. *J. Geophys. Res.*, 114: A00A22, March 2009. https://doi.org/10.1029/2008JA013686.

J. P. Grotzinger, J. Crisp, A. R. Vasavada, R. C. Anderson, C. J. Baker, R. Barry, D. F. Blake, P. Conrad, K. S. Edgett, B. Ferdowski, R. Gellert, J. B. Gilbert, M. Golombek, J. Gómez-Elvira, D. M. Hassler, L. Jandura, M. Litvak, P. Mahaffy, J. Maki, M. Meyer, M. C. Malin, I. Mitrofanov, J. J. Simmonds, D. Vaniman, R. V. Welch, and R. C. Wiens. Mars Science Laboratory Mission and Science Investigation. *Space Sci. Rev.*, 170: 5–56, September 2012. https://doi.org/10.1007/s11214-012-9892-2.

A. M. Gulisano, P. Démoulin, S. Dasso, and L. Rodriguez. Expansion of magnetic clouds in the outer heliosphere. *Astron. Astrophys.*, 543:A107, July 2012. https://doi.org/10.1051/0004-6361/201118748.

J. Guo, M. Dumbović, R. F. Wimmer-Schweingruber, M. Temmer, H. Lohf, Y. Wang, A. Veronig, D. M. Hassler, L. M. Mays, C. Zeitlin, B. Ehresmann, O. Witasse, J. L. Freiherr von Forstner, B. Heber, M. Holmström, and A. Posner. Modeling the Evolution and Propagation of 10 September 2017 CMEs and SEPs Arriving at Mars Constrained by Remote Sensing and In Situ Measurement. *Space Weather*, 16:1156–1169, August 2018a. https://doi.org/10.1029/2018SW001973.

J. Guo, R. Lillis, R. F. Wimmer-Schweingruber, C. Zeitlin, P. Simonson, A. Rahmati, A. Posner, A. Papaioannou, N. Lundt, C. O. Lee, D. Larson, J. Halekas, D. M. Hassler, B. Ehresmann, P. Dunn, and S. Böttcher. Measurements of Forbush decreases at Mars: both by MSL on ground and by MAVEN in orbit. *Astron. Astrophys.*, 611:A79, April 2018b. https://doi.org/10.1051/0004-6361/201732087.

J. Guo, S. Banjac, L. Röstel, J. C. Terasa, K. Herbst, B. Heber, and R. F. Wimmer-Schweingruber. Implementation and validation of the GEANT4/AtRIS code to model the radiation environment at Mars. *J. Space Weather Space Clim.*, 9(27):A2, December 2019. https://doi.org/10.1051/swsc/2018051.

J. S. Halekas, S. Ruhunusiri, Y. Harada, G. Collinson, D. L. Mitchell, C. Mazelle, J. P. McFadden, J. E. P. Connerney, J. R. Espley, F. Eparvier, J. G. Luhmann, and B. M. Jakosky. Structure, dynamics, and seasonal variability of the Mars-solar wind interaction: MAVEN Solar Wind Ion Analyzer in-flight performance and science results. *J. Geophys. Res.*, 122:547–578, January 2017. https://doi.org/10.1002/2016JA023167.

D. M. Hassler, C. Zeitlin, R. F. Wimmer-Schweingruber, S. Böttcher, C. Martin, J. Andrews, E. Böhm, D. E. Brinza, M. A. Bullock, S. Burmeister, B. Ehresmann, M. Epperly, D. Grinspoon, J. Köhler, O. Kortmann, K. Neal, J. Peterson, A. Posner, S. Rafkin, L. Seimetz, K. D. Smith, Y. Tyler, G. Weigle, G. Reitz, and F. A. Cucinotta. The Radiation Assessment Detector (RAD) Investigation. *Space Sci. Rev.*, 170:503–558, September 2012. https://doi.org/10.1007/s11214-012-9913-1.

S. G. Heinemann, S. J. Hofmeister, A. M. Veronig, and M. Temmer. Three-phase Evolution of a Coronal Hole. II. The Magnetic Field. *Astrophys. J.*, 863:29, August 2018a. https://doi.org/10.3847/1538-4357/aad095.

S. G. Heinemann, M. Temmer, S. J. Hofmeister, A. M. Veronig, and S. Vennerstrøm. Three-phase Evolution of a Coronal Hole. I. 360° Remote Sensing and In Situ Observations. *Astrophys. J.*, 861:151, July 2018b. https://doi.org/10.3847/1538-4357/aac897.

V. F. Hess and A. Demmelmair. World-wide Effect in Cosmic Ray Intensity, as Observed during a Recent Magnetic Storm. *Nature*, 140:316–317, August 1937. https://doi.org/10.1038/140316a0.

S. J. Hofmeister, A. Veronig, M. Temmer, S. Vennerstrom, B. Heber, and B. Vršnak. The Dependence of the Peak Velocity of High-Speed Solar Wind Streams as Measured in the Ecliptic by ACE and the STEREO satellites on the Area and Co-latitude of Their Solar Source Coronal Holes. *J. Geophys. Res.*, 123:1738–1753, March 2018. https://doi.org/10.1002/2017JA024586.

R. A. Howard, J. D. Moses, A. Vourlidas, J. S. Newmark, D. G. Socker, S. P. Plunkett, C. M. Korendyke, J. W. Cook, A. Hurley, J. M. Davila, W. T. Thompson, O. C. St Cyr, E. Mentzell, K. Mehalick, J. R. Lemen, J. P. Wuelser, D. W. Duncan, T. D. Tarbell, C. J. Wolfson, A. Moore, R. A. Harrison, N. R. Waltham, J. Lang, C. J. Davis, C. J. Eyles, H. Mapson-Menard, G. M. Simnett, J. P. Halain, J. M. Defise, E. Mazy, P. Rochus, R. Mercier, M. F. Ravet, F. Delmotte, F. Auchere, J. P. Delaboudiniere, V. Bothmer, W. Deutsch, D. Wang, N. Rich, S. Cooper, V. Stephens, G. Maahs, R. Baugh, D. McMullin, and T. Carter. Sun Earth Connection Coronal and Heliospheric Investigation (SECCHI). *Space Sci. Rev.*, 136:67–115, April 2008. https://doi.org/10.1007/s11214-008-9341-4.

B. M. Jakosky, R. P. Lin, J. M. Grebowsky, J. G. Luhmann, D. F. Mitchell, G. Beutelschies, T. Priser, M. Acuna, L. Andersson, D. Baird, D. Baker, R. Bartlett, M. Benna, S. Bougher, D. Brain, D. Carson, S. Cauffman, P. Chamberlin, J.-Y. Chaufray, O. Cheatom, J. Clarke, J. Connerney, T. Cravens, D. Curtis, G. Delory, S. Demcak, A. DeWolfe, F. Eparvier, R. Ergun, A. Eriksson, J. Espley, X. Fang, D. Folta, J. Fox, C. Gomez-Rosa, S. Habenicht, J. Halekas, G. Holsclaw, M. Houghton, R. Howard, M. Jarosz, N. Jedrich, M. Johnson, W. Kasprzak, M. Kelley, T. King, M. Lankton, D. Larson, F. Leblanc, F. Lefevre, R. Lillis, P. Mahaffy, C. Mazelle, W. McClintock, J. McFadden, D. L. Mitchell, F. Montmessin, J. Morrissey, W. Peterson, W. Possel, J.-A. Sauvaud, N. Schneider, W. Sidney, S. Sparacino, A. I. F. Stewart, R. Tolson, D. Toublanc, C. Waters, T. Woods, R. Yelle, and R. Zurek. The Mars Atmosphere and Volatile Evolution (MAVEN) Mission. *Space Sci. Rev.*, 195:3–48, December 2015. https://doi.org/10.1007/s11214-015-0139-x.

C. Kay, M. Opher, and R. M. Evans. Forecasting a Coronal Mass Ejection's Altered Trajectory: ForeCAT. *Astrophys. J.*, 775:5, September 2013. https://doi.org/10.1088/0004-637X/775/1/5.

E. Kilpua, H. E. J. Koskinen, and T. I. Pulkkinen. Coronal mass ejections and their sheath regions in interplanetary space. *Living Reviews in Solar Physics*, 14:5, November 2017. https://doi.org/10.1007/s41116-017-0009-6.

L. Lefèvre, S. Vennerstrøm, M. Dumbović, B. Vršnak, D. Sudar, R. Arlt, F. Clette, and N. Crosby. Detailed Analysis of Solar Data Related to Historical Extreme Geomagnetic Storms: 1868 - 2010. *Sol. Phys.*, 291: 1483–1531, May 2016. https://doi.org/10.1007/s11207-016-0892-3.

M. Leitner, C. J. Farrugia, C. MöStl, K. W. Ogilvie, A. B. Galvin, R. Schwenn, and H. K. Biernat. Consequences of the force-free model of magnetic clouds for their heliospheric evolution. *J. Geophys. Res.*, 112:A06113, June 2007. https://doi.org/10.1029/2006JA011940.

Y. D. Liu, X. Zhao, H. Hu, A. Vourlidas, and B. Zhu. A Comparative Study of 2017 July and 2012 July Complex Eruptions: Are Solar Superstorms "Perfect Storms" in Nature? *Astrophys. J. Suppl.*, 241:15, April 2019. https://doi.org/10.3847/1538-4365/ab0649.

N. Lugaz and C. J. Farrugia. A new class of complex ejecta resulting from the interaction of two CMEs and its expected geoeffectiveness. *Geophys. Res. Lett.*, 41: 769–776, February 2014. https://doi.org/10.1002/2013GL058789.

N. Lugaz, M. Temmer, Y. Wang, and C. J. Farrugia. The Interaction of Successive Coronal Mass Ejections: A Review. *Sol. Phys.*, 292:64, April 2017. https://doi.org/10.1007/s11207-017-1091-6.

J. G. Luhmann, M. L. Mays, Yan Li, C. O. Lee, H. Bain, D. Odstrcil, R. A. Mewaldt, C. M. S. Cohen, D. Larson, and Gordon Petrie. Shock connectivity and the late cycle 24 solar energetic particle events in july and september 2017. *Space Weather*, 16(5):557–568, 2018. https://doi.org/10.1029/2018SW001860. URL https://agupubs.onlinelibrary.wiley.com/doi/abs/10.1029/2018SW001860.

S. Lundquist. On the Stability of Magneto-Hydrostatic Fields. *Physical Review*, 83:307–311, July 1951. https://doi.org/10.1103/PhysRev.83.307.

J. J. Masías-Meza, S. Dasso, P. Démoulin, L. Rodriguez, and M. Janvier. Superposed epoch study of ICME sub-structures near Earth and their effects on Galactic cosmic rays. *Astron. Astrophys.*, 592:A118, August 2016. https://doi.org/10.1051/0004-6361/201628571.

M. L. Mays, A. Taktakishvili, A. Pulkkinen, P. J. MacNeice, L. Rastätter, D. Odstrcil, L. K. Jian, I. G. Richardson, J. A. LaSota, Y. Zheng, and M. M. Kuznetsova. Ensemble Modeling of CMEs Using the WSA-ENLIL+Cone Model. *Sol. Phys.*, 290:1775–1814, June 2015. https://doi.org/10.1007/s11207-015-0692-1.

M. Mierla, B. Inhester, A. Antunes, Y. Boursier, J. P. Byrne, R. Colaninno, J. Davila, C. A. de Koning, P. T. Gallagher, S. Gissot, R. A. Howard, T. A. Howard, M. Kramar, P. Lamy, P. C. Liewer, S. Maloney, C. Marqué, R. T. J. McAteer, T. Moran, L. Rodriguez, N. Srivastava, O. C. St. Cyr, G. Stenborg, M. Temmer, A. Thernisien, A. Vourlidas, M. J. West, B. E. Wood, and A. N. Zhukov. On the 3-D reconstruction of Coronal Mass Ejections using coronagraph data. *Ann. Geophys.*, 28:203–215, January 2010. https://doi.org/10.5194/angeo-28-203-2010.

C. Möstl, M. Temmer, T. Rollett, C. J. Farrugia, Y. Liu, A. M. Veronig, M. Leitner, A. B. Galvin, and H. K. Biernat. STEREO and Wind observations of a fast ICME flank triggering a prolonged geomagnetic storm on 5-7 April 2010. *Geophys. Res. Lett.*, 37:L24103, December 2010. https://doi.org/10.1029/2010GL045175.

C. Möstl, T. Rollett, R. A. Frahm, Y. D. Liu, D. M. Long, R. C. Colaninno, M. A. Reiss, M. Temmer, C. J. Farrugia, A. Posner, M. Dumbović, M. Janvier, P. Démoulin, P. Boakes, A. Devos, E. Kraaikamp, M. L. Mays, and B. Vršnak. Strong coronal channelling and interplanetary evolution of a solar storm up to Earth and Mars. *Nature Communications*, 6:7135, May 2015. https://doi.org/10.1038/ncomms8135.

J. T. Nolte, A. S. Krieger, A. F. Timothy, R. E. Gold, E. C. Roelof, G. Vaiana, A. J. Lazarus, J. D. Sullivan, and P. S. McIntosh. Coronal holes as sources of solar wind. *Sol. Phys.*, 46:303–322, February 1976. https://doi.org/10.1007/BF00149859.

D. Odstrcil. Modeling 3-D solar wind structure. *Adv. Space Res.*, 32:497–506, August 2003. https://doi.org/10.1016/S0273-1177(03)00332-6.

D. Odstrcil, P. Riley, and X. P. Zhao. Numerical simulation of the 12 May 1997 interplanetary CME event. *J. Geophys. Res.*, 109:A02116, February 2004. https://doi.org/10.1029/2003JA010135.

D. Odstrcil, V. J. Pizzo, and C. N. Arge. Propagation of the 12 May 1997 interplanetary coronal mass ejection in evolving solar wind structures. *J. Geophys. Res.*, 110: A02106, February 2005. https://doi.org/10.1029/2004JA010745.

A. Papaioannou, O. Malandraki, A. Belov, R. Skoug, H. Mavromichalaki, E. Eroshenko, A. Abunin, and S. Lepri. On the Analysis of the Complex Forbush Decreases of January 2005. *Sol. Phys.*, 266:181–193, September 2010. https://doi.org/10.1007/s11207-010-9601-9.

M. S. Potgieter. Solar Modulation of Cosmic Rays. *Living Reviews in Solar Physics*, 10:3, June 2013. https://doi.org/10.12942/lrsp-2013-3.

I. G. Richardson. Energetic Particles and Corotating Interaction Regions in the Solar Wind. *Space Sci. Rev.*, 111:267–376, April 2004. https://doi.org/10.1023/B:SPAC.0000032689.52830.3e.

I. G. Richardson. Solar wind stream interaction regions throughout the heliosphere. *Living Reviews in Solar Physics*, 15:1, January 2018. https://doi.org/10.1007/s41116-017-0011-z.

I. G. Richardson and H. V. Cane. Near-Earth Interplanetary Coronal Mass Ejections During Solar Cycle 23 (1996 - 2009): Catalog and Summary of Properties. *Sol. Phys.*, 264:189–237, June 2010. https://doi.org/10.1007/s11207-010-9568-6.

P. Riley, M. L. Mays, J. Andries, T. Amerstorfer, D. Biesecker, V. Delouille, M. Dumbović, X. Feng, E. Henley, J. A. Linker, C. Möstl, M. Nuñez, V. Pizzo, M. Temmer, W. K. Tobiska, C. Verbeke, M. J. West, and X. Zhao. Forecasting the Arrival Time of Coronal Mass Ejections: Analysis of the CCMC CME Scoreboard. *Space Weather*, 16:1245–1260, September 2018. https://doi.org/10.1029/2018SW001962.

Martina Rodari, Mateja Dumbović, Manuela Temmer, Lukas M. Holzknecht, and Astrid Veronig. 3D Reconstruction and Interplanetary Expansion of the 2010 April 3rd CME. *arXiv e-prints*, art. arXiv:1904.05611, Apr 2019.

T. Rollett, C. Möstl, M. Temmer, R. A. Frahm, J. A. Davies, A. M. Veronig, B. Vršnak, U. V. Amerstorfer, C. J. Farrugia, T. Žic, and T. L. Zhang. Combined Multipoint Remote and in situ Observations of the Asymmetric Evolution of a Fast Solar Coronal Mass Ejection. *Astrophys. J. Lett.*, 790:L6, July 2014. https://doi.org/10.1088/2041-8205/790/1/L6.

C. Shen, Y. Chi, Y. Wang, M. Xu, and S. Wang. Statistical comparison of the ICME's geoeffectiveness of different types and different solar phases from 1995 to 2014. *J. Geophys. Res.*, 122:5931–5948, June 2017. https://doi.org/10.1002/2016JA023768.

M. Temmer and N. V. Nitta. Interplanetary Propagation Behavior of the Fast Coronal Mass Ejection on 23 July 2012. *Sol. Phys.*, 290:919–932, March 2015. https://doi.org/10.1007/s11207-014-0642-3.

M. Temmer, B. Vršnak, T. Rollett, B. Bein, C. A. de Koning, Y. Liu, E. Bosman, J. A. Davies, C. Möstl, T. Žic, A. M. Veronig, V. Bothmer, R. Harrison, N. Nitta, M. Bisi, O. Flor, J. Eastwood, D. Odstrcil, and R. Forsyth. Characteristics of Kinematics of a Coronal Mass Ejection during the 2010 August 1 CME-CME Interaction Event. *Astrophys. J.*, 749:57, April 2012. https://doi.org/10.1088/0004-637X/749/1/57.

M. Temmer, M. A. Reiss, L. Nikolic, S. J. Hofmeister, and A. M. Veronig. Preconditioning of Interplanetary Space Due to Transient CME Disturbances. *Astrophys. J.*, 835:141, February 2017. https://doi.org/10.3847/1538-4357/835/2/141.

A. Thernisien. Implementation of the Graduated Cylindrical Shell Model for the Three-dimensional Reconstruction of Coronal Mass Ejections. *Astrophys. J. Suppl.*, 194:33, June 2011. https://doi.org/10.1088/0067-0049/194/2/33.

A. Thernisien, A. Vourlidas, and R. A. Howard. Forward Modeling of Coronal Mass Ejections Using STEREO/SECCHI Data. *Sol. Phys.*, 256:111–130, May 2009. https://doi.org/10.1007/s11207-009-9346-5.

A. F. R. Thernisien, R. A. Howard, and A. Vourlidas. Modeling of Flux Rope Coronal Mass Ejections. *Astrophys. J.*, 652:763–773, November 2006. https://doi.org/10.1086/508254.

M. Tokumaru, D. Satonaka, K. Fujiki, K. Hayashi, and K. Hakamada. Relation Between Coronal Hole Areas and Solar Wind Speeds Derived from Interplanetary Scintillation Measurements. *Sol. Phys.*, 292:41, March 2017. https://doi.org/10.1007/s11207-017-1066-7.

T. Žic, B. Vršnak, and M. Temmer. Heliospheric Propagation of Coronal Mass Ejections: Drag-based Model Fitting. *Astrophys. J. Suppl.*, 218:32, June 2015. https://doi.org/10.1088/0067-0049/218/2/32.

S. Vennerstrom, L. Lefevre, M. Dumbović, N. Crosby, O. Malandraki, I. Patsou, F. Clette, A. Veronig, B. Vršnak, K. Leer, and T. Moretto. Extreme Geomagnetic Storms - 1868 - 2010. *Sol. Phys.*, 291:1447–1481, May 2016. https://doi.org/10.1007/s11207-016-0897-y.

A. Vourlidas, B. J. Lynch, R. A. Howard, and Y. Li. How Many CMEs Have Flux Ropes? Deciphering the Signatures of Shocks, Flux Ropes, and Prominences in Coronagraph Observations of CMEs. *Sol. Phys.*, 284:179–201, May 2013. https://doi.org/10.1007/s11207-012-0084-8.

B. Vršnak, M. Temmer, and A. M. Veronig. Coronal Holes and Solar Wind High-Speed Streams: I. Forecasting the Solar Wind Parameters. *Sol. Phys.*, 240:315–330, February 2007. https://doi.org/10.1007/s11207-007-0285-8.

B. Vršnak, T. Žic, D. Vrbanec, M. Temmer, T. Rollett, C. Möstl, A. Veronig, J. Čalogović, M. Dumbović, S. Lulić, Y.-J. Moon, and A. Shanmugaraju. Propagation of Interplanetary Coronal Mass Ejections: The Drag-Based Model. *Sol. Phys.*, 285:295–315, July 2013. https://doi.org/10.1007/s11207-012-0035-4.

B. Vršnak, M. Temmer, T. Žic, A. Taktakishvili, M. Dumbović, C. Möstl, A. M. Veronig, M. L. Mays, and D. Odstrčil. Heliospheric Propagation of Coronal Mass Ejections: Comparison of Numerical WSA-ENLIL+Cone Model and Analytical Drag-based Model. *Astrophys. J. Suppl.*, 213:21, August 2014. https://doi.org/10.1088/0067-0049/213/2/21.

B. Vršnak, T. Amerstorfer, M. Dumbović, M. Leitner, A. M. Veronig, M. Temmer, C. Möstl, U. V. Amerstorfer, C. J. Farrugia, and Galvin A. B. Heliospheric Evolution of Magnetic Cloud. *Astrophys. J.*, accepted, 2019.

Y. Wang, C. L. Shen, S. Wang, and P. Z. Ye. An empirical formula relating the geomagnetic storm's intensity to the interplanetary parameters: $-\overline{vB_z}$ and Δt. *Geophys. Res. Lett.*, 30:2039, October 2003a. https://doi.org/10.1029/2003GL017901.

Y. Wang, C. Shen, S. Wang, and P. Ye. Deflection of coronal mass ejection in the interplanetary medium. *Sol. Phys.*, 222:329–343, August 2004. https://doi.org/10.1023/B:SOLA.0000043576.21942.aa.

Y. Wang, B. Wang, C. Shen, F. Shen, and N. Lugaz. Deflected propagation of a coronal mass ejection from the corona to interplanetary space. *J. Geophys. Res.*, 119:5117–5132, July 2014. https://doi.org/10.1002/2013JA019537.

Y. M. Wang, P. Z. Ye, and S. Wang. Multiple magnetic clouds: Several examples during March-April 2001. *J. Geophys. Res.*, 108:1370, October 2003b. https://doi.org/10.1029/2003JA009850.

D. Webb and N. Nitta. Understanding Problem Forecasts of ISEST Campaign Flare-CME Events. *Sol. Phys.*, 292:142, October 2017. https://doi.org/10.1007/s11207-017-1166-4.

R. M. Winslow, N. A. Schwadron, N. Lugaz, J. Guo, C. J.
Joyce, A. P. Jordan, J. K. Wilson, H. E. Spence, D. J.
Lawrence, R. F. Wimmer-Schweingruber, and M. L.
Mays. Opening a Window on ICME-driven GCR
Modulation in the Inner Solar System. *Astrophys. J.*,
856:139, April 2018.
https://doi.org/10.3847/1538-4357/aab098.

O. Witasse, B. Sánchez-Cano, M. L. Mays, P. Kajdič,
H. Opgenoorth, H. A. Elliott, I. G. Richardson,
I. Zouganelis, J. Zender, R. F. Wimmer-Schweingruber,
L. Turc, M. G. G. T. Taylor, E. Roussos, A. Rouillard,
I. Richter, J. D. Richardson, R. Ramstad, G. Provan,
A. Posner, J. J. Plaut, D. Odstrcil, H. Nilsson,
P. Niemenen, S. E. Milan, K. Mandt, H. Lohf, M. Lester,
J.-P. Lebreton, E. Kuulkers, N. Krupp, C. Koenders,
M. K. James, D. Intzekara, M. Holmstrom, D. M.
Hassler, B. E. S. Hall, J. Guo, R. Goldstein, C. Goetz,
K. H. Glassmeier, V. Génot, H. Evans, J. Espley, N. J. T.
Edberg, M. Dougherty, S. W. H. Cowley, J. Burch,
E. Behar, S. Barabash, D. J. Andrews, and N. Altobelli.
Interplanetary coronal mass ejection observed at
STEREO-A, Mars, comet 67P/Churyumov-Gerasimenko,
Saturn, and New Horizons en route to Pluto: Comparison
of its Forbush decreases at 1.4, 3.1, and 9.9 AU.
J. Geophys. Res., 122:7865–7890, August 2017.
https://doi.org/10.1002/2017JA023884.

A. M. Wold, M. L. Mays, A. Taktakishvili, L. K. Jian,
D. Odstrcil, and P. MacNeice. Verification of real-time
WSA-ENLIL+Cone simulations of CME arrival-time at
the CCMC from 2010 to 2016.
J. Space Weather Space Clim., 8(27):A17, March 2018.
https://doi.org/10.1051/swsc/2018005.

H. Xie, N. Gopalswamy, P. K. Manoharan, A. Lara,
S. Yashiro, and S. Lepri. Long-lived geomagnetic storms
and coronal mass ejections. *J. Geophys. Res.*, 111:
A01103, January 2006.
https://doi.org/10.1029/2005JA011287.

T. H. Zurbuchen and I. G. Richardson. In-Situ Solar Wind
and Magnetic Field Signatures of Interplanetary Coronal
Mass Ejections. *Space Sci. Rev.*, 123:31–43, March 2006.
https://doi.org/10.1007/s11214-006-9010-4.